POLITECNICO
MILANO 1863

SCUOLA DI ARCHITETTURA URBANISTICA
INGEGNERIA DELLE COSTRUZIONI

A PFEM numerical study of 3D concrete printing in a lunar environment

Tesi di Laurea Magistrale in
Ingegneria dei sistemi edilizi

Author: **Elena Martinazzoli**

Student ID: 250677
Advisor: Prof. Massimiliano Cremonesi
Co-advisors: Giacomo Rizzieri
Academic Year: 2025-26

Abstract

3D concrete printing (3DCP) coupled with In-Situ Resource Utilization (ISRU) drastically reduces material transport costs from Earth for lunar construction. However, reduced gravity (1.62 m/s^2) poses significant challenges. This thesis investigates 3DCP applicability on the Moon, analyzing how modified gravity, rheology, and process variables affect deposition dynamics and structural stability. In the absence of physical experimentation in the lunar environment, numerical simulations using the Particle Finite Element Method (PFEM) are performed. Fresh concrete behavior is modeled by comparing the Bingham and Saramito models to accurately capture free-surface flows and large deformations. Parametric analyses assess the influencee of yield stress and shear modulus during free-flow deposition and layer pressing, while buildability tests explore vertical development limits before collapse. Results show that lunar gravity strongly attenuates filament slumping, making yield stress requirements less stringent than on Earth. Crucially, layer pressing emerges as the optimal strategy, ensuring better adhesion and allowing the printing of structures over twice as tall as terrestrial ones. This work provides a robust numerical framework for rheological design and optimization of construction processes in an extraterrestrial environment.

Keywords: 3D concrete printing (3DCP); Lunar construction; PFEM; Rheology; Buildability; Layer pressing.

Abstract in lingua italiana

La stampa 3D del calcestruzzo (3DCP) con impiego di risorse in loco (ISRU) riduce notevolmente i costi di trasporto dei materiali dalla Terra per le costruzioni lunari, ma affronta la sfida della gravità ridotta (1.62 m/s^2). Questa tesi indaga l'applicabilità della 3DCP sulla Luna, analizzando l'impatto di gravità, reologia e parametri di processo su deposizione e stabilità strutturale. In assenza di sperimentazione fisica in ambiente lunare, si ricorre a simulazioni numeriche tramite il Metodo degli Elementi Finiti a Particelle (PFEM). Il calcestruzzo fresco è modellato confrontando i modelli di Bingham e Saramito per gestire grandi deformazioni e flussi a superficie libera. Analisi parametriche valutano la tensione di snervamento e il modulo di taglio in modalità flusso libero e pressatura (layer pressing), mentre test di costruibilità determinano i limiti di sviluppo verticale prima del collasso. I risultati indicano che la gravità lunare riduce drasticamente il cedimento (slump) dei filamenti: i requisiti reologici risultano quindi meno stringenti che sulla Terra. Il layer pressing emerge come strategia ottimale, garantendo maggiore adesione e permettendo di stampare strutture alte più del doppio rispetto a quelle terrestri. Questo studio fornisce un solido framework numerico per la progettazione reologica e l'ottimizzazione dei processi costruttivi in ambiente extraterrestre.

Parole chiave: Stampa 3D del calcestruzzo (3DCP); Costruzione lunare; PFEM; Reologia; Costruibilità; Layer pressing.

Contents

Introduction

3D Concrete Printing (3DCP) is an innovative technology for automated construction. It produces building components by depositing material layer by layer. This process relies on a digital model, which is developed using advanced digital modeling and toolpath-generation software to guide the fabrication of the structure.

This technique represents a substantial change from traditional construction methods and aims to automate the construction sector with its potential for rapid industrialization. This is made possible by the ability to achieve greater efficiency in terms of time, labor use, and related costs, and by reducing material waste through the production of optimized geometries in which material is placed only where it is structurally required. Although the environmental impact depends primarily on the mix used, this technology favors eliminating the use of formwork; this latter aspect also allows for the creation of more complex geometries [1][2][3].

Furthermore, this technology aims to improve productivity and safety in the construction industry by offering the ability to operate in hazardous environments without the need for direct human intervention. As a result, it can reduce the rate of accidents on construction sites due to the complexity of construction processes by minimizing direct human labor [4].

Printing process and materials

The 3DCP process occurs by dispensing the cementitious material through a printer, typically consisting of a material preparation unit, namely the mixer, the transport pump, and a deposition system, called the nozzle (Figure 1) [5].

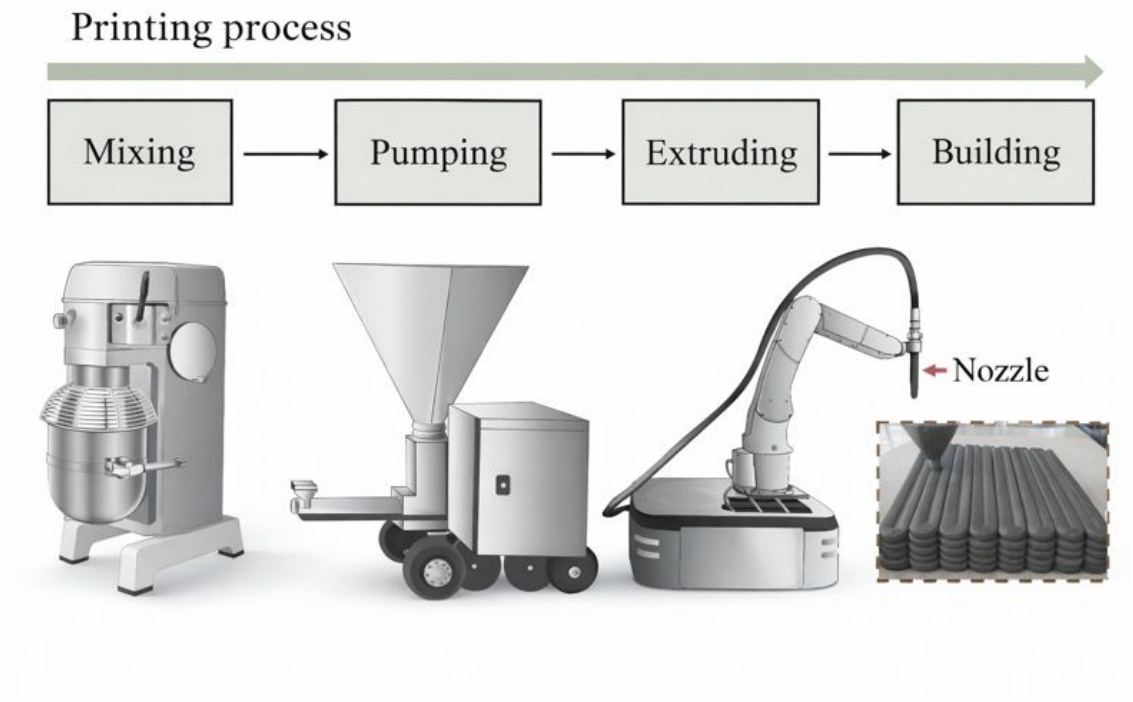

Figure 1: Steps of the printing process[6].

Nozzle handling depends on the type of motion control system; there are mainly three types: gantry systems, robotic arms, and cranes (Figure 2). Gantry and crane systems are ideal for the ability to create large structures, while the robotic arm allows for greater flexibility in creating complex geometries [1].

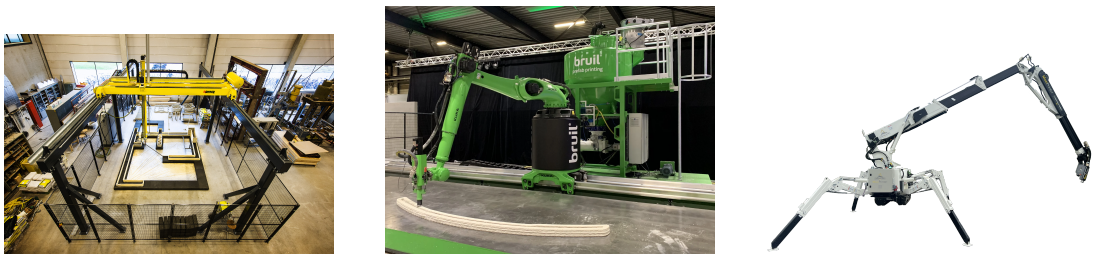

(a) Gantry system. (b) Robotic arm. (c) Crane.

Figure 2: The three different types of 3D printing systems [7].

The chosen structure model can have great geometric freedom; however, for this capability to be feasible, gantry systems require 3 or 4 degrees of freedom, while robotic arms offer up to 6, varying depending on the type of kinematics and extrusion nozzle [8].

Digital modelling is performed through specific software that allows one to draw any necessary element. The actual printing of the material is done by layers of material, called beads, placed one on top of the other [9]. The path followed by the nozzle is constructed using Cartesian coordinates and printing parameters, including printing speed, extrusion speed, and printing diameter, which will be determined by the diameter of the nozzle from which the material exits.

Path design is very important because, in addition to creating the correct geometry, it is necessary to prevent collisions between the machine itself and the previously deposited layers; for this aspect, digital simulation of the paths is essential, which ensures the feasibility and safety of the manufacturing process [2].

To print correctly, a balanced combination of all the values given to the machine is therefore necessary, based on the desired geometry, the quality of the material used, and the environment in which it is printed [1].

The type of nozzle is very important as this is the element that determines the

printing of the material, its deposition and therefore the shape of the structure to be created.

In this regard, it is very important to evaluate the nozzle geometry: square or rectangular shapes provide a larger contact area than circular ones, improving adhesion between adjacent layers and promoting constructability [1]. The nozzle also affects the surface finish of the printed concrete. Different finishes can be achieved by using nozzles equipped with steering and shaping blades, which smooth the material between layers and reduce surface roughness [8]. In addition to the finish, the shape of the nozzle influences the deposition of the material itself, determining the stability of the freshly extruded filament.

Furthermore, regarding the characteristics of the nozzle, it is important to evaluate its height, i.e. the distance between the nozzle and the construction surface, to ensure that adhesion between the layers occurs correctly [10].

Clearly, in addition to the configuration of the printing system, it is very important for this technology to evaluate the properties of the material. The material used is a mixture that must meet various requirements even in the fresh state to be printed. There are three main ones: pumpability, i.e. the ease with which the material is transported, extrudability, i.e. the ability to be delivered through the nozzle as a continuous filament and constructability, i.e. the ability to support its own weight and that of subsequent layers without collapsing or excessively deforming [11].

All three of these requirements depend on the characteristics of the concrete. An example of this is hydration; the mixture, to ensure that a proper bond is created between one layer and another and at the same time remains workable, must have controlled hydration [12].

The main aspect that differentiates the material used in 3D printing is precisely this, and it is called “open time”: that is, the time window during which the material

maintains the ability to be successfully printed before it solidifies. It is the critical and most important aspect to evaluate when choosing the characteristics of concrete.

Thixotropy is an essential property, as the material must behave like a fluid during movement and, once molded, must quickly acquire strength to support the next layer or layers. This behaviour is controlled by viscosity, the property of matter that describes the internal resistance of a fluid to flow, and depends mainly on the water/binder ratio that must be properly balanced. Finally, the material must possess a high static viscosity at rest but become less viscous when stressed during pumping and finally quickly regain its viscosity once extruded [1].

To better control the behaviour of the material in receiving the next layer, it is necessary to choose the correct timing between the printing of the layer and when it receives the next layer; if the time is too long, a so-called "cold joint" is created, meaning poor adhesion occurs and an interface is weakened. This phenomenon accentuates the anisotropic behaviour of the printed structure: unlike traditional cast-in-place concrete, which is isotropic, the printed mixture has mechanical properties that vary depending on the direction of load application, which is less resistant at the interface between the layers [13].

To achieve these characteristics, the mixture is characterised by a high content of binders and fine aggregates. Regarding binders, silica fume, fly ash or ground granulated blast furnace slag (GGBS) is often incorporated [11]. When it comes to aggregates, great attention must be paid to their size. Large aggregates can create blockages inside the machine if the nozzle diameter is not large enough.

A final aspect to be evaluated when choosing the characteristics of the mixture is the presence of short fibres, such as steel, glass or polymers, to ensure ductility and control the formation of shrinkage cracks or fissures. This aspect is very important because there is currently no standardized automation for the insertion of steel bars,

which provide tensile strength in reinforced concrete. Therefore, there is a tendency to add these fibers or manual positioning of the steel bars between the layers; at the same time, systems are being developed that can also automate this step using additional robots that have the ability to position continuous reinforcements, such as steel wires or cables [14].

Some existing pilot projects

Although 3DCP is not yet widespread, there are some notable pilot projects that represent the technical applicability and construction potential of this technology.

Two-story building in China

The first project analyzed is a two-story building constructed in China (Figure 3), developed through the study of a systematic workflow for digital design and in-situ printing [15].

The construction process was divided into several steps; the design phase involved converting the planned structure into substructures compatible with printability constraints and choosing the optimal nozzle path. Subsequently, the digital computation phase was addressed with the generation of the machine control code for the printable components and the choice of process parameters. To validate this, simulations and tests were carried out to confirm the printing parameters and stability of the printed beads. The final steps were the construction phase, which took place on site, including the preparation of equipment, materials, and real-time monitoring and control systems.

The building has a height of 6 meters and a surface area of 52.8 m^2. The chosen structure is of the hybrid type: with a reinforced concrete frame, with columns and beams, combined with 3D-printed walls, a solution chosen to comply with existing local regulations.

The printed walls have variable geometries, some are linear partitions 250 mm thick, while others are curved walls 400 mm thick. From a material perspective, two mixtures were used: the first characterized by the presence of a coarse aggregate, a density of 2350 kg/m^3 and a compressive strength of 53.6 Mpa; the second with a fine aggregate and a density of 2270 kg/m^3 and a compressive strength of 48.7 Mpa.

Both include Class 42.5 cement, polypropylene (PP) fibres and specific additives.

The use of a coarse aggregate was chosen to improve adhesion between layers and reduce anisotropy.

Regarding the printing parameters, a portal printing machine (gantry) of on-site assemblies was chosen, because it can support the printing of large models. Two different nozzles were used to extrude the different mixtures, due to the presence of coarse aggregate in one of them; the printing head also included a vibration and mixing system to ensure pumpability over long distances and promote cohesion between the layers.

The deposited beads had a width of 50 mm and a height of 20 mm, with a printing speed between 4500 and 7500 mm/min. The time interval between layers (between 13 and 17 minutes) was also carefully monitored to avoid the formation of cold joints.

The construction process followed an iterative sequence for the two levels of the building: vertical reinforcing bars were inserted every 500 mm and horizontal meshes were added every 100 mm, integrating traditional methods into the automated process. Subsequently, prefabricated lintels were laid for the door and window openings, and sheet metal sheets for the attic. During construction, a movable cover was installed to protect the print from rain and high summer temperatures, ensuring controlled environmental conditions.

Construction was successfully completed, and there were no excessive errors that were not immediately corrected, such as collapses and route deviations, thanks in part to continuous monitoring.

Figure 3: Panoramic photograph of the 3D printed two-story building.

Office of the Future in Dubai

A second relevant structure is the project "Office of the Future" (Figure 4), built in Dubai, United Arab Emirates in 2016: an office building with a surface area of 185 m^2 [16].

This case study, unlike the previous one, was not printed on site, but was printed in different components using a robotic arm printer in China and then assembled in a few days on site on cast-in-place foundations.

A comparison of the two methodologies shows that on-site printing reduces transportation costs and logistical challenges and allows for larger units, but factory prefabrication ensures a controlled environment and better-quality control.

The structure was entirely 3D printed, except for the foundations. To facilitate transport and respect the printer's limitations, it was divided into 6 parts. The printing geometry was chosen based on the printer's capabilities and the model's needs: the extruded beads had a width of 50 mm and a height of 20 mm. To ensure an optimal connection between the segments, the joints were filled and, during printing, steel reinforcement was inserted between the layers.

The construction process was developed in several phases: initially the model was designed, then subdivided to adapt it to the selected printer; subsequently the printing of the model. Once completed, the structure was shipped and, once it reached the installation site, it was checked, verified and modified where necessary. Finally, it was mounted on the cast-in-place foundations; the various parts of the structure were joined together and finished by adding grouting and non-structural finishing layers.

This project is an important example that represents the possible use of 3D concrete printing, but at the same time highlights the need for improvements. In fact, once the construction was completed, tests were performed due to the uncertainty about the mixture, the chosen printing dimensions and the adhesion between the reinforcement and the concrete.

The tests revealed some problems, because the thickness was not constant, but varied between 35 and 45 mm and the failure mechanism was influenced by the adhesion between the steel and the concrete, particularly in the upper layers, because in the lower layers it was better due to the weight of the upper layers. To overcome these problems, an external transverse post-tension was added to help improve flexural capacity.

These errors highlight the need to apply improvements such as increasing the quality of the concrete mix, implementing more control procedures and developing connection details between different parts of the structure during the printing process.

Figure 4: 3D printed office during applying the external finishing.

Pedestrian bridge in Nijmegen

A third project that shifts the application of 3D printing to infrastructure is a pedestrian bridge (Figure 5) in Nijmegen, in the Netherlands, an unreinforced arch structure with a total span of 29 m [17].

The bridge's geometry is divided into five spans, 4.5 to 6.5 m long, 3.5 m wide, and 0.7 to 1.2 m high. These spans are further divided into smaller elements: two lateral support elements (columns) and the central element, which are assembled later for production and logistics reasons. The central element has the particularity of not being full-section, but made up of different "bottle-shaped" elements connected to each other; this solution was adopted to reduce the overall weight of the structure and allow the passage of the post-tensioning cables.

The static principle behind this design uses arc-shaped and post-tensioning to keep the material constantly compressed. This design strategy addresses the limited tensile strength of concrete and the difficulty of automatically integrating the reinforcement during 3D printing.

The mixture used is a premixed, single-component cement powder, with microfibers, silica fume, and additives to control viscosity.

In this study, the construction process is different, because before arriving at the construction of the complete bridge, several phases were carried out to demonstrate the applicability of 3D printing in the infrastructure sector. First, parametric design was developed to define the bridge geometry and the subdivisions required for printing; subsequently, a single representative full-scale span was created to identify and verify potential critical issues.

This span was subjected to bending and shear tests to determine the ultimate design load. Once the results of these tests were obtained, all parts of the bridge were printed and it was assembled.

In addition to the span built just to carry out the checks, other checks were carried out on both the material and the assembled bridge. Tests on the material used were performed to verify the anisotropic behavior of the printed concrete, while tests on the assembled bridge covered each span, loaded up to the final design load without causing damage to the structure.

This last example highlights an aspect that had not been addressed in previous cases, namely that infrastructure structures can also be built using 3D printing of concrete, provided that the construction process includes careful checks of structural behaviour and performance quality.

Figure 5: Assembly of the final bridge on location.

3D printing on the Moon

While terrestrial 3D printing challenges focus primarily on optimizing complex geometries and material rheology under standard gravity, the application of this technology in the lunar environment presents a different set of extreme environmental challenges. The Moon represents a key point for exploring the solar system, the closest place to Earth and an ideal location for testing extraterrestrial construction technologies. The main goal is to establish a sustainable presence by building on-site facilities, reducing costs, time and launch volume constraints [18]. It is estimated that transporting a single brick to the Moon costs up to $2 million [19].

Consequently, a permanent lunar base cannot depend solely on terrestrial supplies: the goal is to reduce this dependence by applying the strategy of using resources that can be found directly on the Moon [18]. The use of 3D printing technology is essential to exploit local materials and minimize human intervention, the on-site support of which would be excessively risky and costly.

In addition to evaluating the use of materials, it is important to analyze the constraints imposed by the environment in which one operates. Lunar geological and environmental conditions differ dramatically from Earth's. An advantageous aspect is the lunar gravity, equal to 1.62 m/s^2, compared to 9.81 m/s^2 on Earth. This means that the load capacity can be up to six times higher than on Earth, allowing for a simpler structural design without the need for ultra-high strength materials [20]. Furthermore, thanks to the reduced gravity and modest lunar seismic activity, the maximum recorded magnitude is 4.1; therefore, the structural risk is considered manageable with standard design criteria [20].

The Moon has no atmosphere, which exposes the surface to microasteroids [20]. The absence of atmosphere also has a beneficial effect on structural performance, as it eliminates lateral loads due to wind and disruptions caused by precipitation, which

therefore do not have to be considered in the structural calculation [19].

A negative aspect of the absence of an atmosphere is the presence of a high vacuum, which causes chemical-physical problems. In particular, liquid evaporation occurs almost instantly, making the use of hydraulic systems in printing robots inadvisable and complicating the management of fluid binders [20]. This last point can also negatively influence the curing processes of the material, which risks drying out in a way that does not comply with the expected conditions [19].

Thermal conditions on the Moon are extremely critical, temperatures ranging from about -244° C, in permanently shaded areas, up to +122° C, in areas near the equator, with day-night cycles of 14 Earth days. These thermal variations can cause thermal shock, stress, deformation and fatigue in both printed materials and robotic equipment, which therefore must be adequately protected from both temperature changes and extreme thermal conditions [20]. The curing processes, in addition to the absence of atmosphere, are also influenced by these thermal conditions: excessive heat can cause drying too quickly, while cold can stop the process [19]. Attention must be paid to exposure to cosmic radiation, which is dangerous for both humans and the robots' electronics [19] [21].

The lunar illumination cycle also imposes severe constraints on energy replenishment. Since transporting fuels from the Earth is difficult and the use of combustion generators is impossible in the absence of an atmosphere, the robots' power supply is mainly based on photovoltaic solar energy combined with storage systems, namely batteries. However, the long lunar night, approximately 354 hours, represents a critical issue: current battery technology barely provides enough energy to keep the printing process running for two weeks without solar charging. Consequently, the operational strategy must be carefully planned to concentrate the construction phases during the illumination period, providing for hibernation or thermal maintenance phases during the lunar night.

The construction strategy is based on the use of lunar regolith, the surface is completely covered by regolith. It is a non-consolidated, cohesive and angular material, with a thickness ranging from 2-4 m in the seas to 6-8 m in the highlands; and inside it can contain various minerals [20]. Thanks to the characteristics of this regolith, deep foundations are not necessary, but it is sufficient to level and sinter the surface, to implement support bearings, or use anchors, with cables into the ground, to counteract tensile loads [20].This is because the regolith is very compact under the first 30 cm and excessive digging would require the implementation, and related transportation, of heavy machinery.

In addition, the choice to print with lunar regolith allows the structure itself to have effective shielding against radiation [22]. The mixture for 3D printing on the Moon is made of regolith combined with binders and solvents [23]. However, under reduced gravity, adhesion between layers is critical and porosity may increase due to the irregular shape of the regolith. The use of thin layers improves mechanical properties, but lengthens execution times. Since on-site testing is impossible, research relies on the use of regolith simulants on Earth, systems that allow the chemical-physical properties of the lunar regolith to be replicated, to validate the mixtures before the mission [24] [19].

As for automation, it is not sustainable on the Moon to carry gantry systems that are too large and heavy. It is necessary to design the construction mode through the use of swarms of smaller, more compact mobile robots that can work in parallel, speeding up construction. However, this requires complex coordination to avoid collisions and optimize routes [20]. Robots must be designed to withstand environmental characteristics. Regolith is fine, abrasive, and electrostatically charged, tending to adhere to all surfaces, even mechanical ones, causing frictional wear. Therefore, electrostatic cleaning systems, Teflon coatings, or magnetic filters are needed to protect their mechanisms [18]. They require thermal overhang shielding and armor plates, or safety offsets, to protect against any micrometeorite impacts

during printing [20]. In a vacuum, heat dissipation occurs only through conduction and radiation, limiting the efficiency of cooling systems and reducing the energy required for thermally activated processes [20].

Finally, given the communication delay and limited human presence, monitoring the robot's process is crucial. The system must be very reliable, fault-tolerant, and capable of autonomously detecting anomalies to activate countermeasures. The current monitoring model is based on the comparison between the two-dimensional images that can be acquired during printing and the created digital model. For each layer, different geometric indices are calculated and analyzed, in order to diagnose any anomalies as a function of the type of error, by evaluating the specific tolerance ranges [24].

1 | Material for Lunar 3D Printing

Although the goal of a permanent base is established, there is still a lack of a suitable building material, producible with lunar resources and capable of withstanding extreme environmental conditions [25].

The main challenges, as mentioned above, are the vacuum environment, which causes the mixing water to evaporate rapidly, making the material porous; low gravity, which can reduce friction by 10%; and the absence of an atmosphere, as there is only a thin exosphere that does not protect against meteorite and micrometeorite impacts. Furthermore, the temperature is critical, as there is a 14-day day-night cycle with an extreme temperature range, and the presence of radiation (GCR), due to galactic cosmic rays and energetic solar particles (SEP) [25].

It is necessary to consider water-free concrete or low-water-content concrete and use in situ resources (ISRU), since the transport of aggregates, water and cement from Earth is not feasible. Consequently, an in-depth analysis of lunar regolith is required [26].

1.1. Lunar Regolith

The main material present is lunar regolith, a silty sand with a grain size between 46 and 110 μm, composed of sharp, glassy grains similar to volcanic ash. Geologically, the crust divides into seas (basaltic) and plateaus (feldspathic) [25].

Understanding the mechanical and rheological properties of regolith is critical to the success of missions to rocky bodies, including sample collection, in situ resource utilization (ISRU), and planetary defense [27].

The regolith covers the lunar surface with a thickness of 3-20 m and is formed by meteorite impacts and solar wind.

Regolith is rich in aluminosilicates (SiO_2 40-50%). There are differences between samples from the highlands and the seas.

The samples from the highlands are richer in aluminum (28%, Si/Al ratio 1.5) and calcium (17%, Si/Ca ratio 2.6), while those from the seas have less aluminum (12%, Si/Al ratio 3.4) and less calcium (10%). In the highlands the content of amorphous substances (31-36%) is significantly higher than that of the seas, making them better precursors to obtain high mechanical performance [28].

Figure 1.1: Detail of lunar regolith grains: angular, irregular fragments resulting from impact crushing processes.

1.1.1. Regolith simulants

Due to cost, time, and waste, materials simulating lunar regolith were created to test printability. Various types have been developed from different raw materials, all of which aim to recreate the limited properties of material brought back directly from the moon.

The most popular is the JSC-1A simulant, a later version of the JSC-1. JSC-1A simulates a low-titanium "sea" regolith and is mined from a volcanic ash deposit near Flagstaff, Arizona [29].

JSC-1A is a ground basaltic tuff that replicates the mineralogical chemistry and engineering properties of the original lunar samples. It is a multicomponent material, consisting of phenocrysts of olivine (9%), plagioclase (37%), pyroxene and titanium-rich magnetite, embedded in a volcanic glass matrix (about 50%) with minor oxide phases [30]. The powder was sieved to obtain particles smaller than 125 μm, resulting in a particle size distribution with $d(0.5)$ of 75 μm, similar to that of sub-millimeter lunar soil samples [31].

To test its potential as a substitute for original regolith, several comparative analyses were performed. The measured specific gravity, which indicates the ratio of the solid material's density to that of water, is 2.92, comparable to the JSC-1 value of 2.90 and the range 2.9-3.4 of the Apollo samples. The density was found to be consistent with in situ density estimates. Particle size analysis shows that JSC-1A does not contain particles larger than 1.18 mm and faithfully follows the upper limit of the particle size curves of the samples for the coarser fractions (>0.20 mm). Scanning electron microscope (SEM) analysis reveals very angular particles with rough surfaces, classified as sub-prismoidal. This morphology is due to the grinding process and closely resembles that of the real lunar regolith [29].

Tests were then carried out to verify the mechanical characteristics. A triaxial compression test was performed to measure the constitutive behavior of the material and its stress-strain behavior was analyzed. Two different specimens were analyzed, one with a lower density, $1.63 g/cm^3$, to give a "loose" packing and one with a higher density, $1.88 g/cm^3$, to give a dense consistency. These were tested at different pressures.

Loose samples initially show contraction, followed by dilatancy (volumetric expansion) which reaches a maximum at peak stress. While at very low pressures (10 kPa), the behavior is dilatant from the beginning. The dense samples show a marked peak strength followed by a softening associated with the formation of shear bands. The volumetric response shows a small initial contraction followed by dilatancy. The high angularity of the particles leads to the formation of shear bands [29].

Another simulant used is TUBS-I (developed by TU Braunschweig), a mixture of basalt and anorthosite that replicates the chemical and mineralogical properties of the lunar soil (sea and highland regions) and whose average grain size is 87 μm [32].

An additional material used is BH-1, a simulant that faithfully replicates the real

lunar regolith collected in terms of chemical composition, mineralogy, reflectance spectrum and microscopic characteristics, indeed the chemical composition shows minimal differences, less than 5

Finally, HIT-LRS-1 was used, it was created by grinding with anhydrous alcohol in a planetary ball mill of starting materials such as basalt, plagioclase, forsterite, albite, ilmenite and hematite, mixed in specific ratios, and subsequently dried [33].

1.1.2. Behavior of simulants in different environments

In addition to considering individual mechanical properties, since the environment is different, it is necessary to evaluate the impact of reduced gravity on mechanical properties. This has practical consequences for construction: light machinery, to reduce launch costs, will have less traction due to reduced gravity and will have to operate on soil with much greater shear strength and dilatancy than expected, reducing the efficiency of excavation and earthmoving operations.

These simulants, while having optimal characteristics on Earth, will perform differently in reduced gravity, making extrapolations based on ground-based tests for the design of space systems unreliable. For example, a parametric analysis with respect to the two environments, terrestrial and lunar, relating to the flow during the printing process, demonstrates that for the same cohesion the flow velocity decreases with decreasing gravity, due to the reduced gravitational force, and variations in the friction coefficient do not change the shape of the flow profile, except for wall effects at low friction values [27].

Another typical characteristic of the material that varies greatly depending on the environment in which it is printed is dilatancy, that is, the property of some granular materials and some substances (such as concentrated suspensions) which, under certain conditions, behave like moderately viscous liquids, while in others, as they harden, they assume an almost solid consistency.

Dilatancy, representing the increase in volume during shear, is a crucial aspect at low stresses [34].

The shear strength of a granular material is described by the equation:

$$\tau = c + \sigma \tan(\phi)$$

Where σ is the normal stress.

The strength properties of granular materials in low-gravity, low-stress environments differ significantly from the predictions of conventional geotechnical engineering. Shear strength is dominated by particle interlocking and resulting dilatancy, leading to friction angles much higher than those measured at high stresses [34].

These results are critical for the design of regolith landing, excavation, and handling systems (including 3D printing) on the lunar surface, where material strength may be higher than previously estimated.

A fundamental concept in granular rheology is the competition between intergranular forces (cohesive) and external forces (gravity), often described by the dimensionless granular Bond number (Bo). However, the use of Bo has limitations since the macroscopic behavior depends on bulk properties and the polydispersity of minerals and grain sizes, which can lead to very different rheological responses [27].

1.2. Classification of printing materials

The main requirements for building materials to be used in lunar environments include durability, ductility, vapor impermeability, high tensile and compressive strength, and low coefficient of thermal expansion [25].

Given the composition of regolith, several processes have been studied to treat it to form the mixture suitable for structural 3D printing. Some examples are sintering processes, via microwave or laser, the production of molten basalt, polymerization and the use of sulfur-based binders.

1.2.1. Sintering

A first example of regolith treatment is sintering, it is done between 1000 and 1100°C, but tests have shown limited compressive strengths [25].

1.2.2. Molten basalt

Molten basalt, on the other hand, shows better mechanical properties, and good moldability. However, it has shrinkage problems during the cooling phase, which lead to the presence of many cracks, and is extremely fragile and difficult to machine [25].

1.2.3. Metal extraction and thermite reaction

Tests have also been performed on metals, such as aluminum, iron, magnesium, and titanium, which are present in large quantities in the form of oxides. A thermite reaction between regolith and aluminum powder has been studied, despite requiring the import of large quantities of metal powder. After initial ignition, the produced samples showed low compressive strength and defects due to incomplete reaction in vacuum [25].

1.2.4. Sulfur-based concrete

Another type of material that can be recreated using regolith is sulfur-based material. Sulfur, present in regolith (0.16-0.27%) is extractable by heating the material to 1100°C, and can act as a binder without the use of water. Sulfur concrete hardens quickly and resists chemicals well. However, this solution also requires modification with polymers to be transported from Earth to avoid cracking due to volumetric expansion, of about 7%, during cooling. Another critical limit is the sublimation of the binder in vacuum; in fact, at 120°C a 1 cm layer sublimates in less than 2 hours. Furthermore, thermal cycling causes surface cracking due to the difference in thermal expansion coefficients between sulfur and aggregates, reducing compressive strength [25].

Concrete has excellent compressive strength but poor tensile strength, which traditionally requires steel bars. An alternative method of increasing tensile strength is the use of glass or steel fibers. Since fiberglass can be produced directly from the silica present in regolith, its production is achievable with simple processes and can be effective for both concrete reinforcement and post-tensioning cable production [26].

1.2.5. Polymer Concretes

Then there are polymer concretes, which use resins or thermoplastic materials as a binder for regolith (containing up to 90% filler). Experiments with lunar simulants and polyethylene or other polymers have shown good mechanical strengths. The main problem remains the unavailability of polymers on the Moon and the need to transport them entirely from Earth, as well as the lack of data on long-term behavior in a vacuum [25].

1.2.6. Ice composites

Alternative techniques, such as mixing pulverized ice and cement in a vacuum with subsequent microwave thawing, have produced materials with high void content (11%). In fact, a crucial discovery concerns the presence of water: the LCROSS mission detected water ice in the regolith of craters constantly in shadow, thus indicating that processes should not be limited to anhydrous processes, that is, processes devoid of water. However, linked to this material there is the limit of evaporation due to vacuum [25].

While water can be obtained from regolith or ice at the poles, the amount needed to activate traditional cement would make costs prohibitive. An alternative to cement concrete is the use of polymers or resins that replace cement as a binder [26].

1.2.7. Low-temperature method

Another type of lunar regolith processing is low-temperature deposition (material extrusion, geopolymers) [35]. This method offers moderate compressive strength with low energy consumption, but presents challenges related to binder dependence and instability in vacuum.

It is a technique that involves the deposition of a concrete-like slurry composed of regolith powder that solidifies through drying or polymerization. It can occur through the use of different materials such as thermoplastic filaments, sulfur, which allows for faster processing than thermoplastics, or liquid binders, deposited on layers of powder, which allow for high resolution and complex geometries.

Low-temperature methods excel in energy efficiency but are limited in ISRU compatibility.

1.2.8. High-energy method

Then there is a high-energy additive beam manufacturing method, involving melting on a powder bed and directly depositing energy [35]. This technique involves binder-free fabrication, which is better for in situ resource utilization (ISRU), although they suffer from porosity, high energy intensity, and geometric limitations. It consists of two main methods of sintering and casting.

High-energy methods offer binder-free fabrication at the cost of high energy intensity.

1.2.9. Soft inks

A particular method, but different from the most common methods used, is 3D printing of "soft" inks. It is an important technique because it introduces elastic/flexible materials, which are rare in the lunar context.

The goal is to create robust and elastic architectures using liquid inks based on lunar regolith simulant particles, 3D printed by extrusion at ambient conditions. The result is a composite material, consisting of approximately 90% regolith by weight and 10% a biodegradable elastomer (PLGA), which responds to the need for "soft" materials for extraterrestrial applications [23].

The inks are synthesized, the composition includes three main components: the powder, involving commercial sieved simulants JSC-1A (lunar), the elastomeric binder, polylactic-co-glycolic acid (PLGA) and the solvent mixture, formed by dichloromethane (DCM) as the main evaporant, 2-butoxyethanol (2-Bu) as surfactant and dibutyl phthalate (DBP) as plasticizer.

Crude powders, which show an irregular and jagged morphology, contain particles up to 1 mm, requiring sieving (approximately 45 μm) to remove coarse fractions that prevent extrusion through nozzles $<$ 2 mm.

The final ink formulation involves a solids loading of 70-75 vol% regolith and 30-25 vol% PLGA.

Rheologically, it shows similar shear-thinning behavior, indicating that the flow properties are independent of the specific morphology of the particles. The inks are stable and can be stored for months.

Liquid inks can be rapidly 3D printed in linear deposition rate of up to $150/s$. Solidification occurs rapidly due to evaporation of the DCM, eliminating the need for post-process drying times.

Adhesion of the first layer is critical, especially under low gravity conditions; the use of sandpaper or silicon carbide as a substrate ensured effective adhesion while allowing for easy removal of the object.

The process is compatible with a wide range of nozzle diameters (330 μm - 1.4 cm) and extrusion pressures ($100-550$ kPa). The ink is also extrudable through 330 μm nozzles.

This versatility allows ranging from high-resolution printing to large-volume deposition (up to $1^3/h$ theoretical with large nozzles).

Microscopic analysis reveals distinct internal and external microstructures. The interior is characterized by a dense distribution of particles connected or encapsulated by a continuous network of PLGA elastomer. The porosity of the material is $27.9 \pm 4.4\%$, independent of the nozzle diameter. While the exterior has a thin (< 5 μm) and poorly porous PLGA "skin", formed by the rapid evaporation of the solvent on the exposed surface.

The residual solvent in the freshly extruded ink locally dissolves the PLGA of the previously deposited layers, creating seamless physical transitions between layers. This feature is essential to ensure structural integrity. The microstructure also

allows for post-printing processes such as solvent polishing or cutting.

The materials exhibit mechanical behavior dominated by the continuous elastomeric matrix, despite the high percentage of rigid particles.

In tension the material supports significant deformations before failure, with an elastic range of 15-20%, it exceeds 250% deformation without failure. And it has a good response to cyclic behavior, samples can undergo cyclic deformations, up to 100% extension, without fracturing or showing substantial fatigue, although net shape recovery is limited if 15-20% deformation is exceeded.

This method is also designed for sustainability in resource-constrained environments.

Regolith is collected in situ and sieved, elastomer (PLGA) can be synthesized from monomers derived from biological waste (e.g. urine, compost) and among the solvents DCM evaporates and must be captured and recycled for safety reasons; it can be synthesized from methane and chlorine, while 2-Bu and DBP can be recovered by washing the molded parts with ethanol and subsequent fractional distillation.

1.2.10. Laser fusion

The laser additive manufacturing methodology was evaluated via an experiment conducted with a Selective Laser Melting machine (SLM100A, Realizer GmbH) equipped with a ytterbium-doped fiber laser ($\lambda = 1.06\ \mu m$) with a maximum power of 50 W [31].

Process parameters, related to the laser, controlled included scanning speed (u), hatch spacing (h), laser power (P), beam diameter (δ), and layer thickness (t).

The resulting microstructure is characterized by rapid melting and solidification. Cooling rates up to $10^5\ ^\circ C\ s^{-1}$ favored glass formation (vitrification). However, the

angular morphology of the particles and the resulting suboptimal packing, together with partial energy absorption, hindered complete solidification, leading to low-density parts compared to conventional vitrification.

The stress-strain curves obtained are those typical of brittle and porous materials (such as ceramic foams). A direct linear correlation was observed between laser energy density and mechanical properties: higher energy led to denser struts between the pores and therefore higher strength [32].

The maximum strength of 4.2 MPa is comparable to that of clay bricks (3.5 MPa) and, considering the reduced lunar gravity, would be as structurally effective as concrete blocks on Earth [31].

Regarding flow properties, understanding viscosity is critical for process operations involving molten regolith flow, such as material delivery in extrusion-based 3D printing techniques and melt infiltration into porous structures [30].

The results indicate that the molten simulant exhibits Newtonian behavior throughout the analyzed temperature range ($1200 - 1600°C$). This means that the dynamic viscosity is independent of the applied shear rate [30].

Thus, the viscosity decreases approximately exponentially as the temperature increases. However, smaller discrepancies were detected between the measured data and the theoretical values at $1225°C$ and $1600°C$; it is hypothesized that at temperatures below $1250°C$ an onset of crystallization may occur, although the behavior remains Newtonian. Temperature control is critical for maintaining a constant flow during 3D printing, including for energy efficiency, because radiative losses are significant; minimizing the exposed surface area of ducts and tanks is critical for energy balance [30].

1.3. Geopolymers

Alkali-activated geopolymers are inorganic polymeric materials formed by the depolymerization and subsequent polymerization of aluminosilicates in an alkaline environment.

These materials represent the closest solution to traditional terrestrial concrete in terms of process and performance.

Lunar regolith, being composed mainly of aluminosilicate minerals (over 80%) and containing an amorphous phase between 10% and 36%, possesses properties similar to common terrestrial geopolymer precursors. This technology allows for a high degree of use of local resources and low energy consumption, since the water required for the reaction can be extracted and recycled [28].

They are sustainable inorganic materials based on aluminosilicates [36].

Geopolymers are amorphous ceramic systems produced by alkalizing natural or waste substances. However, developing geopolymer blends for AM is complex: the paste must be thixotropic, showing good flowability before extrusion (low dynamic yield stress) and excellent stacking characteristics after extrusion (high static yield stress) [36].

The main advantages of geopolymers include high compressive strength,which can reach 15-30 MPa after 4 hours of treatment at room temperature; rapid curing; high-temperature resistance; and high resistance to acid attack, such as corrosion. however, there are challenges such as the variability of raw materials, the dependence of viscosity on temperature, the brittleness of the material and the high cost of alkaline activators [36].

For 3D printing, geopolymers must meet specific rheological, physical, and mechanical parameters, influenced by raw material composition, activators, reinforcements,

and curing conditions.

In the fresh state, the main rheological characteristics that geopolymers pastes have are fluidity, essential for pumping and extrusion during the printing process. In fact, the correct balance between fluidity, therefore a low dynamic viscosity, and constructability, therefore another yield stress, is necessary. Extrudability is also important for obtaining a continuous filament during printing and depends on the ratio between the components of the mixture and in particular on the particle size distribution of the aggregates. While in the hardened state there are other important properties. One is density, 3d printing can lead to having low density, due to void formation, high pressure extrusion helps improve it [36].

Then there are the mechanical properties of geopolymers which show anisotropic behaviour, that is, the longitudinal direction (parallel to the print) always has a higher resistance than the lateral or perpendicular directions. This is due to the presence of voids and weak adhesion between layers. However, heat treatment and the use of reinforcements (such as continuous micro-cables or short fibers) can significantly increase flexural strength and load-bearing capacity.

Fibers can reduce adhesion between layers if not aligned correctly or if they excessively increase the stiffness of the mixture. Low temperature and high humidity environmental conditions can deteriorate the interface between the layers [36].

1.3.1. Geopolymerization process

Geopolymerization is a chemical-physical process that transforms aluminosilicate materials (natural or industrial waste, such as fly ash or blast furnace slag) into solid, resistant, ceramic-like materials through a reaction with an alkaline aqueous solution (activator), forming a polymer gel that acts as a binder, all at low temperatures (below 100°C).

The chemical ratios of highland regolith are more suitable for geopolymerization, favoring superior pozzolanic activity [28]. In fact, the highland regolith behaves like a mixed system.

The reaction process is divided into four phases: depolymerization, involving the dissolution of the amorphous constituents (CaO, SiO_2, Al_2O_3) into free ions by the OH^- ions; condensation, that is, the formation of condensation gels and CSH gels with the intervention of Na^+ and Ca^{2+} ions; the addition of Al^{3+}, that is, the aluminate ions replace the hydroxyl groups forming Si-O-Al bonds and the product (N,C)-ASH; and finally the formation of the shell, involving the precipitation and hardening of the shell of reaction products [28].

Among the various technologies proposed (high-temperature sintering, sulfur concrete), geopolymerization offers significant advantages thanks to the mechanical strength, thermal insulation and radiation protection of the produced materials. Geopolymers are formed by combining an aluminosilicate precursor (such as regolith) with an alkaline activator [37].

Geopolymer concrete solidifies to form a gel matrix composed mainly of hydrated calcium silicate (CSH), hydrated sodium aluminosilicate (NASH) and hydrated calcium aluminosilicate (CASH), which bind the particles [28].

In a specific study, the alkaline activator may be composed of pure sodium hydroxide and distilled water. The thixotropic agent Attagel-50 (an attapulgite composed of magnesium aluminosilicate hydrate with median particles of 9 μm) and polypropylene (PP) fibers with a length of 3 mm and a diameter of 32 μm were used as rheological modifiers [37].

For the mixture under examination, the static yield stress (τ_s) was measured, calculated by applying an increasing linear strain (0.1 s^{-1}) after a pre-shear. A higher value indicates better constructibility; the dynamic yield stress (τ_0) and the plas-

tic viscosity (μ), determined via increasing and decreasing flow curves (from 0 to 100 s^{-1}), interpolating the data with the Bingham model ($\tau = \tau_0 + \mu\dot{\gamma}$). These parameters influence the extrudability.

Two methods have been adopted to improve printability. Adjusting the printing temperature, taking advantage of the thermosensitivity of the geopolymer, the paste is kept fluid in the tank (at low temperature) and heated in the printing chamber or during extrusion to accelerate hardening and improve constructability. Water/binder (W/B) ratios of 0.30 and 0.32 were tested at temperatures of 40, 60, and 80°C. and the use of additives, the amounts of Attagel-50 (0.3%, 0.5%, 1.0%) and PP fibers (1.0%, 1.5%, 2.0%) with a fixed W/B ratio of 0.32 were varied to evaluate their rheological impact.

The printed samples ($40 \times 40 \times 160$ mm) were cured for 72 hours under simulated lunar temperature and vacuum conditions. Different filling paths (infills) were tested: wave, fast honeycomb and straight with angles of 30°, 45° and 90°. The bending and compressive strengths were measured in different loading directions (X, Y, Z) to evaluate the anisotropy [37].

The main factors influencing the mechanical properties are: the content of amorphous substances, a higher content favors their reactivity, such as a higher presence of molten basalt shows a higher compressive strength than untreated crystalline basalt, at 7 days 12.1 MPa versus 3.37 Mpa; the chemical composition, and therefore the balance between the ratio between the elements is important, The addition of inert powders or a change in particle size affects the reaction, finer particles will allow for a specific surface area, larger and with higher reactivity; activators also have a significant impact, high alkalinity can worsen mechanical properties, generally an optimal value is between 4 and 12

The influence of some values was then verified. Increasing the Water/Binder W/B ratio reduces the static yield stress (τ_s), the dynamic yield stress (τ_0) and the plastic

viscosity (μ). A higher water content decreases the solid volume fraction and internal friction, facilitating extrusion but penalizing constructability due to the reduction of τ_s.

The addition of PP fibers significantly increases τ_s (+72.9% with 2.0% fibers), improving the ability to maintain shape due to the fiber bridging effect that delays gel breakage. τ_0 and μ also increase with fiber content, as these act as a second dispersed phase that increases internal friction. Attagel-50 significantly increases τ_s (up to 3.65 times with 1% addition), promoting constructability. However, it also increases τ_0, which can reduce extrudability. Compared to the W30 control group, the addition of 0.3% Attagel to the W32 group (ATT0.3%) produced a similar τ_s but with lower values of τ_0 and μ, suggesting better extrudability for the same constructibility.

Temperature dramatically influences the temporal evolution of rheological parameters. τ_s, τ_0, and μ increase with time, and temperature accelerates this growth by promoting geopolymerization and free water consumption. This rapid increase of τ_s at high temperature is advantageous for post-extrusion constructability.

Increasing the temperature reduces the open time. With a W/B of 0.30 at 60°C and 80°C, the open time is less than 10 minutes, making extrusion difficult. With a W/B of 0.32, the open time is adequate (>20 min) even at higher temperatures. A W/B of 0.28 caused nozzle blockages, while a W/B of 0.34 produced a paste that was too fluid and unable to hold its shape.

An upper threshold for extrudability has been identified: pastes are extrudable if $\tau_0 \leq 3116$ Pa and $\mu \leq 33.08$ Pa s. These values delimit the workability area for the printing system used.

Stacking tests showed that the number of printable layers before collapse increases with printing temperature. The W32T80 group (W/B 0.32 at 80°C) reached 33 lay-

ers, compared to 7 in the W30T40 group, demonstrating that heating promotes the rapid hardening required for vertical stability. This combination optimally balances extrudability, open time and constructability.

Constructibility is related to the static yield stress τ_s. It has been determined that to ensure good constructability, the material must have an initial τ_s or a specific growth rate. For the heated process (W32T80), an initial τ_s of 2039.8 Pa and a growth rate of 135.6 Pa/min were identified as minimum requirements.

For scenarios where thermal control is not feasible, a blend (ADM) for printing at $20°C$ was optimized by adding 0.3% Attagel-50 and 0.5% PP fibers at a W/B ratio of 0.32. This mixture showed optimal rheological parameters (τ_0 and μ within the extrudability limits, τ_s above the constructibility limit) and an open time extended to over 40 minutes, allowing for easy and stable printing even at room temperature.

Of the various filling paths tested, the straight one (rectilinear) proved to be the best, avoiding defects and gaps typical of wiggle or honeycomb paths. The optimal orientation angle (routing angle) was found to be $\pm 45°$, which maximizes both flexural and compressive strength with respect to the $\pm 30°$ and $\pm 90°$ angles.

The printed samples show marked anisotropy. Maximum mechanical strengths were obtained by loading along the Z-direction (perpendicular to the layers), reaching 4.1 MPa in bending and 48.1 MPa in compression after 72 hours of curing in a simulated lunar environment. Although lower than the mold-cast samples, these values are promising considering the reduced lunar gravity (1/6 of Earth's).

Geopolymers hold up well at extreme temperatures, even after thermal cycling they retain 90% of the residual strength [28]. Geopolymers show good resistance to cosmic radiation. The shielding capacity increases linearly with the density of the material. Regolith covers of more than 1 meter reduce radiation by more than 50% [28].

Compared to techniques such as sintering and casting (energizing) or the use of terrestrial binders (expensive transportation), geopolymers offer low energy consumption and high in situ resource utilization. Water can be recycled and the process lends itself to automated 3D printing [28].

1.3.2. Tested structure via geopolymerization

An example of a structure made with geopolymerization is a "zigzag" structure [33].

The geopolymer ink was obtained by activating the simulant with a solution of alkali silicate precursor (mixture of NaOH and silica sol). The powder and solution were mixed in a 1:1 ratio at $0°C$ to obtain a homogeneous slurry. Printing was performed with a 0.82 mm nozzle at a speed of 40 mm/s, followed by curing at $65°C$ for 24 h.

The rheological properties (viscosity, storage and loss modulus, yield stress) and phase structure were evaluated by X-ray diffraction (XRD). The microstructure was analyzed by SEM and EDS, while the porosity was analyzed by image analysis software. The mechanical properties (compressive strength, Young's modulus) were tested on printed samples. Thermal conductivity was measured with a Laser Flash analyzer and solar reflectivity by a UV/vis spectrometer.

Additionally, finite element simulations (FEM) were performed to investigate the mechanical and thermal transport properties of the printed structures. Uniform stress was applied to the upper surface of the modeled structures, keeping the base fixed, to analyze compressive strength and load distribution.

The simulant shows a mineralogical composition similar to real lunar soil (trevorite, pyroxene, forsterite, etc.) and an amorphous phase rich in Si and Al (29.2 wt%) suitable for geopolymerization and contains the formation of the three-dimensional Si-O-Al-O network typical of geopolymers. Microscopically, the geopolymer consists of an amorphous matrix encapsulating randomly distributed Fe_2O_3 microflakes and

SiO_2 nanocrystals.

From a rheological point of view, the slurry shows shear-thinning behavior (viscosity decreases as the shear rate increases), facilitating extrusion. The minimum yield stress (τ_0) is 7188.7 Pa, the point at which the material transitions from solid to liquid, allowing the shape to be maintained after deposition. Oscillation tests confirm a rapid and reversible strain-controlled solid-liquid-solid transition, ideal for printing.

A porous layered architecture with a zigzag pattern was designed, composed of a wavy interlayer (semicircles) and outer layers of different shapes (semicircle, triangle, rectangle, scale). The fracture mechanism is pseudo-plastic and progressive ("graceful failure"): cracks begin at the edges and propagate layer by layer, allowing stress relaxation. FEM simulations confirm that the triangular structure distributes the load more evenly, contributing to structural stability, while the semicircular interlayers improve toughness.

Thermal insulation is important to maintain habitat at $20°C$ against lunar temperature variations. The zigzag structure reduces the equivalent thermal conductivity to about 0.2 W/m K at $25°C$ (half that of the dense material), due to air trapped in the pores and the elongation of the thermal diffusion path.

However, the lunar geopolymer strongly absorbs solar radiation (absorbance 0.85) due to iron oxide, bringing the daytime surface temperature to about $112°C$.

To address this, an iron-free geopolymer (cGP) coating was developed. This coating has high reflectivity in visible light (bright white color) due to the absence of Fe_2O_3 and the presence of micropores that cause backscattering of the light; and maintains high emissivity in the infrared (> 0.93), promoting radiative cooling.

Solar simulator tests showed that the cGP coating reduced surface temperature by approximately $51.5°C$ compared to the uncoated geopolymer, lowering the energy

requirement for thermal conditioning of the habitat.

1.4. Comparative assessment of lunar 3D printing materials and techniques

In the previous sections, the main materials and different methodologies for lunar 3D printing were examined. Although each method demonstrates interesting potential, none can currently be considered universally optimal. A critical comparison is therefore needed to evaluate their mechanical performance, energy demand, compatibility with in situ resource utilization (ISRU), environmental resistance, and process feasibility under lunar conditions.

High-temperature methods such as sintering, molten basalt processing, and laser melting offer the advantage of binder-free fabrication and strong ISRU compatibility. However, they require extremely high energy consumption and often result in high porosity and brittleness. Furthermore, thermal gradients and radiative losses in vacuum complicate temperature control.

Sulfur-based and polymeric concretes reduce water dependence, addressing the problem of vacuum-induced evaporation. However, sulfur presents problems with sublimation and thermal cracking, while polymer concretes rely heavily on materials that must be transported from Earth, reducing sustainability.

Low-temperature extrusion methods, especially geopolymers, represent a promising compromise. They enable high mechanical performance, relatively low energy consumption and partial ISRU integration. However, they require alkaline activators and rheological control to ensure printability and adhesion between layers.

Soft regolith-based inks introduce flexibility and damage tolerance, rare features in extraterrestrial building materials. Despite their mechanical advantages in terms of deformability, their dependence on polymers and solvents poses logistical and

sustainability challenges.

From a structural and construction prospective, geopolymer-based systems currently appear to offer the best balance between mechanical strength, energy efficiency, and compatibility with automated extrusion-based printing processes. However, their long-term durability under thermal cycling and radiation exposure has yet to be validated.

Table **??** summarizes the main characteristics, advantages and limitations of each method, highlighting the different solidification principles and material requirements.

Table 1.1: Summary and comparison of lunar 3D printing methods.

Method	**Materials**	**Solidification / Hardening Principle**	**Advantages**	**Limitations**
Sintering (microwave/ thermal)	Regolith	Thermal fusion (1000–1100°C)	No binder, ISRU compatibility	High energy demand, limited compressive strength, porosity
Molten Basalt	Melted regolith/basalt	Thermal melting and solidification	Good moldability, improved strength	Shrinkage cracking, brittleness, high thermal gradients
Laser Fusion (SLM)	Regolith powder	Localized laser melting and vitrification	High geometric precision, no binder	Porosity, energy-intensive, brittle behavior

Table 1.1 – continued from previous page

Method	Materials	Solidification / Hardening Principle	Advantages	Limitations
Thermite reaction / Metal extraction	Regolith + imported Al powder	Exothermic chemical reaction	Metal production potential	Requires imported metals, low mechanical performance
Sulfur-based concrete	Regolith + sulfur	Thermal melting and cooling crystallization	Low water need, fast setting	Sublimation in vacuum, thermal cracking, volumetric expansion
Polymer concrete	Regolith + polymer resin	Polymerization (chemical curing)	High mechanical strength, low water need	Polymers must be imported, unknown long-term vacuum durability
Ice composites	Regolith + water/ice	Freezing / phase change	Potential in polar regions	High porosity, evaporation risk in vacuum
Low-temperature extrusion	Regolith + binder	Drying / polymerization	Energy efficient	Binder dependency, vacuum instability
High-energy beam methods	Regolith	Direct energy melting	ISRU compatibility	Very high energy consumption, porosity

Table 1.1 – continued from previous page

Method	Materials	Solidification / Hardening Principle	Advantages	Limitations
Soft inks (PLGA-based)	Regolith + elastomer + solvent	Solvent evaporation	Elastic behavior, damage tolerance	Polymer and solvent logistics, sustainability issues
Geopolymers	Regolith + alkaline activator	Alkali activation (chemical geopolymerization)	High compressive strength, moderate energy, ISRU compatibility	Requires activators, rheological control critical, anisotropy

2 | Numerical simulations of 3D printing

Numerical validation of the project is performed through computational simulations. The main advantages of this approach are the ability to test the influence of different combinations of printing parameters and rheological properties of concrete without the need for a physical printer. The goal of the simulations is, therefore, to predict the outcome of the printing process to conduct analyses to achieve the desired filament shape, and subsequently perform physical production.

Before detailing the simulation setup, it is necessary to introduce the numerical framework adopted to simulate the 3D printing process [38].

2.1. Theoretical model

Numerical simulation techniques for 3DCP can be categorized into three main groups: discrete methods, continuum solid and fluid single-phase approaches. The latter two model the material as a homogeneous continuum, while discrete approaches represent it as a set of interacting discrete elements.

Fresh concrete is a dual-phase material, a fluid and granular material, due to the mixture of particles and aggregates suspended in a fluid matrix. Given this nature, it is possible to use both continuum and discrete numerical simulation approaches [39].

3DCP process is divided into several phases, involving different physical phenomena and characteristic dimensions. The most relevant steps are mixing, pumping, extrusion, layer

deposition, stability and shape maintenance of the extruded element. Therefore, it is justified to consider fresh concrete as a continuum and treated as a homogeneous viscous fluid [40].

Based on this hypothesis, the single-phase fluid model is adopted, treating the material as an incompressible fluid governed by the Navier-Stokes equations, which are a system of partial differential equations that account for the conservation of momentum, mass and energy in fluid dynamics, solved by CFD methods, such as FEM.

Standard CFD simulations take an Eulerian approach; the equations are governed on a fixed computational grid. This method can be advantageous because it avoids problems due to mesh distortion and allows for simplified management of inflow and outflow boundary conditions. This allows for large deformations, but managing evolving domains remains difficult and interfaces, such as the concrete-air interface of 3D printing.

In this work, a Lagrangian framework is preferred over Eulerian or ALE approaches. A key advantage of the Lagrangian description is that it naturally tracks the free surface of the material without requiring additional capturing techniques, which is fundamental for simulating the deposition process in 3D printing.

Assuming the fluid to be homogeneous, isothermal, and incompressible, the governing equations are the momentum balance and mass continuity equations. In the Lagrangian reference frame, where the mesh nodes follow the material particles (i.e., the convective velocity is null), the total time derivative coincides with the local derivative. The governing equations read:

$$\rho \frac{d\mathbf{u}}{dt} = \nabla \cdot \boldsymbol{\sigma} + \rho \mathbf{b} \quad \text{in } \Omega_t \times [0, T] \tag{2.1}$$

$$\nabla \cdot \mathbf{u} = 0 \quad \text{in } \Omega_t \times [0, T] \tag{2.2}$$

where:

- ρ is the fluid density (assumed constant for incompressible flow);
- $\mathbf{u} = \mathbf{u}(\mathbf{x}, t)$ is the velocity field;
- $\boldsymbol{\sigma} = \boldsymbol{\sigma}(\mathbf{x}, t)$ is the Cauchy stress tensor;
- $\mathbf{b}$ is the vector of body forces (e.g., gravity).

The Cauchy stress tensor $\boldsymbol{\sigma}$ is typically decomposed into a volumetric part (dependent on pressure p) and a deviatoric part ($\boldsymbol{\tau}$):

$$\boldsymbol{\sigma} = -p\mathbf{I} + \boldsymbol{\tau} \tag{2.3}$$

where $\mathbf{I}$ is the identity tensor.

To solve these equations, a suitable constitutive law relating the deviatoric stress $\boldsymbol{\tau}$ to the deformation of the material is required.

2.2. Bingham constitutive law

The rheological behavior of fresh concrete is characterized by the existence of a yield stress [41], consisting of a stress threshold that separates the perfectly rigid behavior of the material from the regime of the flowing fluid.

Consequently, in addition to the reference equations, it is necessary to define a non-Newtonian rheological law that represents this behavior of the material. The rheological behavior of fresh concrete is often modeled with Bingham's law, which is written as:

$$\boldsymbol{\tau}(\boldsymbol{u}) = 2\mu\boldsymbol{\epsilon}(\boldsymbol{u}) + \tau_0 \frac{\boldsymbol{\epsilon}(\boldsymbol{u})}{\|\boldsymbol{\epsilon}(\boldsymbol{u})\|} \tag{2.4}$$

Where:

- $\boldsymbol{\tau}$ is the deviatoric stress tensor
- μ is the fluid plastic viscosity
- τ_0 is the yield stress
- $\boldsymbol{\epsilon}(\boldsymbol{u})$ is the deviatoric strain rate

Yield stress represents a sharp discontinuity that can cause numerical implementation problems. Therefore, an exponential approximation of (2.4) is adopted to avoid instabilities and convergence problems:

$$\boldsymbol{\tau}(\boldsymbol{u}) = \left[2\mu + \frac{\tau_0}{\|\boldsymbol{\epsilon}(\boldsymbol{u})\|}\left(1 - e^{-m\|\boldsymbol{\epsilon}(\boldsymbol{u})\|}\right)\right]\boldsymbol{\epsilon}(\boldsymbol{u}) \tag{2.5}$$

Where $m = 1000$ s is set to reproduce the real law also at lower strain rates.

This model treats the material as a rigid solid when the stress is below τ_0 and as a viscous fluid when it exceeds it.

2.3. Saramito constitutive law

While the Bingham model captures the viscoplastic nature of concrete, it neglects the elastic deformation that occurs before yielding. To describe the material behavior more accurately, specifically its transition between a solid-like elastic state and a fluid-like viscous state, the elasto-viscoplastic (EVP) model proposed by Saramito [42] [43] is adopted.

This model is derived from thermodynamic principles and allows for a smooth transition between the solid and fluid regimes. It combines the viscoelastic properties (Oldroyd-B type) with a yield stress criterion. In this framework, the deviatoric stress tensor $\boldsymbol{\tau}$ is split into two contributions: a solvent part (Newtonian) and a polymer part (viscoelastic/plastic):

$$\boldsymbol{\tau} = 2\eta_s \dot{\boldsymbol{\epsilon}} + \boldsymbol{\tau}_p \tag{2.6}$$

Where:

- η_s is the solvent viscosity (representing the Newtonian matrix);
- $\boldsymbol{\tau}_p$ is the polymeric stress tensor (representing the microstructure);
- $\dot{\boldsymbol{\epsilon}}$ is the strain rate tensor.

The evolution of the polymeric stress tensor $\boldsymbol{\tau}_p$ is governed by the Saramito constitutive equation. The numerical implementation of the Saramito model adopted in this thesis follows the approach proposed in [44]. In the Lagrangian framework adopted for this work, the convective term in the upper-convected derivative vanishes, simplifying the equation to a system of Ordinary Differential Equations (ODEs) at each material point:

$$\frac{d\boldsymbol{\tau}_p}{dt} - \boldsymbol{\tau}_p \cdot \nabla \mathbf{u} - (\nabla \mathbf{u})^T \cdot \boldsymbol{\tau}_p + \frac{\alpha_{sar}}{\lambda} \boldsymbol{\tau}_p = 2G\dot{\boldsymbol{\epsilon}} \tag{2.7}$$

Where:

- G is the elastic shear modulus;
- $\lambda = \eta_p/G$ is the relaxation time, with η_p being the polymer viscosity;
- α_{sar} is a coefficient that introduces plasticity based on the von Mises yield criterion.

The plasticity coefficient α_{sar} is defined as:

$$\alpha_{sar} = \max\left(0, \frac{||\boldsymbol{\tau}_p|| - \tau_0}{||\boldsymbol{\tau}_p||}\right) \tag{2.8}$$

This function controls the state of the material:

Where:

- When $||\boldsymbol{\tau}_p|| \leq \tau_0$, then $\alpha_{sar} = 0$. The material behaves as a Kelvin-Voigt viscoelastic solid.
- When $||\boldsymbol{\tau}_p|| > \tau_0$, then $0 < \alpha_{sar} < 1$. The material yields and flows like a viscoelastic Oldroyd-B fluid with an apparent viscosity.

This model requires four parameters: the total viscosity ($\eta = \eta_s + \eta_p$), the shear modulus (G), the yield stress (τ_0), and the ratio between solvent and polymer viscosities. It provides a robust description of materials like fresh concrete that exhibit instantaneous elasticity, creep, and yield stress.

2.4. Particle Finite Element Method (PFEM)

As mentioned above, the Particle Finite Element Method (PFEM) was chosen for its ability to effectively model free-surface flows and large-displacement problems. PFEM addresses this challenge by discretizing the continuum with a finite element mesh where the nodes coincide with the particles of the material fluid.

PFEM is a powerful numerical technique for solving fluid flow problems involving large deformations, free surfaces, and complex boundary conditions [38]. The key concept of PFEM is the integration of FEM with an efficient remeshing procedure.

The model treats the material as a collection of particles, where each particle represents a point in the domain. The particles move according to the governing equations, and the mesh is continuously updated based on the particle positions. Whenever the Lagrangian motion of the nodes results in an excessively distorted mesh, this is discarded, and a new mesh is generated using the same set of nodes. As illustrated in Figure 2.1 (adapted from [45]), the standard PFEM solution cycle involves the following main steps:

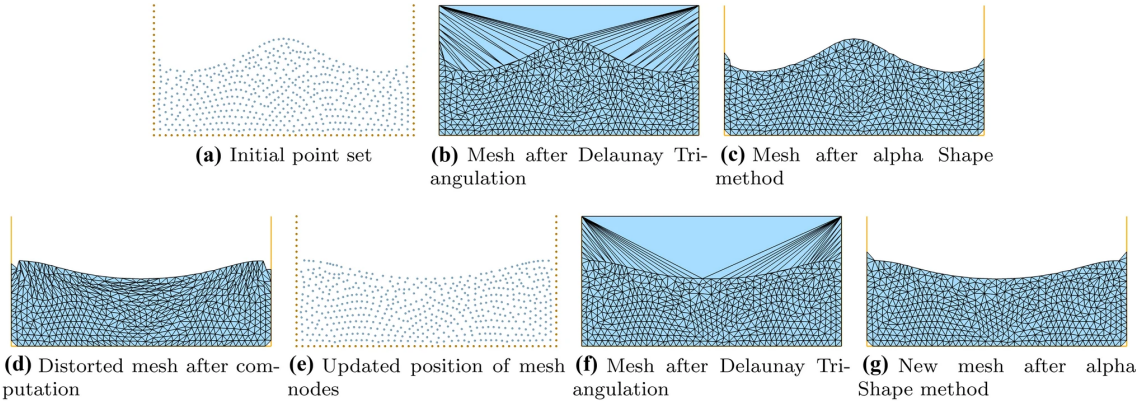

Figure 2.1: Steps of the Particle Finite Element Method (PFEM) solution cycle. Adapted from [45].

1. Particle generation: the domain is discretized into particles representing material points (Figure 2.1a);

2. Mesh generation: a finite element mesh is generated by triangulating the particle

cloud and exploiting the α-shape method (Figure 2.1b-c);

3. Solution of governing equations: the governing equations are solved using the FEM on the mesh (Figure 2.1d);

4. Mesh update: after solving, the particle positions are updated based on the solution (Figure 2.1e-g), and if necessary the mesh is reformed.

Recently, PFEM has been adopted to simulate 3DCP processes, proving the efficiency in predicting the filament shape and the extrusion forces at the nozzle exit [38]. Thixotropic effects were also successfully introduced, highlighting the differences between the final object shapes when time-dependent properties are considered and when they were not [46].

3 | Combined effect of material/process and modified gravity on filament shape

This chapter presents the numerical simulations conducted to analyze the combined effects of material properties, printing process variables, and gravitational conditions on the extrusion and deposition of the filaments.

In the first part of the chapter, the main parameters considered during the study are defined. Subsequently, the results of the simulations are presented and compared, evaluating the material behavior.

3.1. Investigation parameters

To carry out the tests during the project, several parameters were varied, including material properties (yield stress, shear modulus, and plastic viscosity) and printing characteristics (nozzle diameter and height, printing velocity, and extrusion velocity), as well as environmental parameters and boundary conditions.

3.1.1. Material properties

To understand the material behavior during the printing process, it is fundamental to analyze its rheological and mechanical properties. The following parameters define the material's ability to be extruded and to maintain its shape once deposited, directly influencing the buildability of the structure.

Yield stress is the minimum stress that causes the fluid flow as a viscous material, to which the material changes character if force is increased or decreased. This minimum level of stress depends on the stress history of the cementitious materials [47] [48].

In printing, therefore, it represents the stress threshold beyond which the material begins to flow, a high value will simulate a stiffer material, while a low value will simulate a fluid material.

Shear modulus describes the elastic properties of a material under the application of transverse internal stresses. It is a measure of a material's ability to resist transverse deformations and is a representative parameter of the elastic behavior only within the linear elastic regime, during which the material is able to return to its original configuration [49].

In 3D printing this parameter has effects on the mechanical characteristics of the element. A high shear modulus leads to greater structural stiffness, while a low shear modulus leads to greater deformability. While the latter may provide higher flexibility and delay brittle failure, it can also result in geometric instability of the printed layers.

3.1.2. Printing parameters

Alongside the rheological properties of the mixture, the proper calibration of the printing equipment is a determinant factor for the quality of the final structure. This section describes the geometric and kinematic variables of the extrusion system (Figure 3.1) that must be calibrated to control the resolution, stability, and adhesion of the printed layers.

The nozzle diameter is defined as a function of the filament size required for printing: a larger diameter allows for thicker filament, reducing the number of layers required and facilitating the inclusion of coarse aggregates. However, increasing the diameter requires a higher yield stress to ensure filament continuity, a condition that can complicate the mix design and material extrudability [50].

The choice of nozzle height allows for layers with different characteristics. In general, as the nozzle height decreases, the material tends to flow laterally, producing wider, flatter layers, with possible instability or failure in the underlying layers. Conversely, increasing nozzle heights can lead to discontinuous deposition of the material [50].

Printing velocity is the speed with which the nozzle moves, while flow velocity refers to the amount of material that is released through the nozzle over a period of time. Through some studies it is known that, when the printing velocity is lower than the flow velocity, the cross-section of the filament tends to widen, increasing the width of the layer at the expense of height. Conversely, a higher printing velocity can cause progressive thinning and, in the most extreme cases, filament tearing.

Instead, if the two velocities are equal, a nominal process is reproduced, therefore it is the ideal case in which the quantity of material that is extruded in one second covers exactly the distance that the nozzle travels at that moment [50].

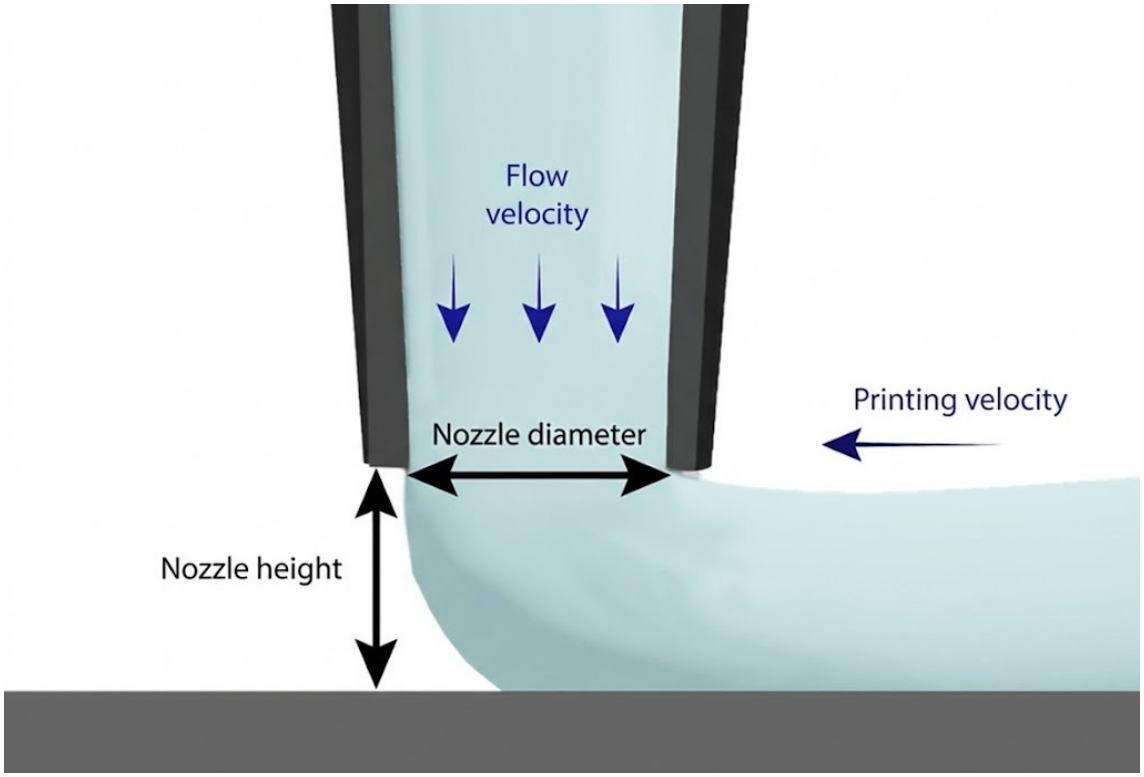

Figure 3.1: Illustration of printing parameters [51].

3.1.3. Environment parameters

The environmental context plays a decisive role in the deposition dynamics. The analysis considers external forces acting on the fresh material, specifically focusing on the gravitational differences between terrestrial and lunar scenarios.

Gravity (g) is important for its effect on force. Weight can be defined as the force of gravitational attraction on the object; that is, how heavy it is and how much it depends on gravity. Weight is also defined as the force with which a body is attracted to the Earth or another celestial body, equal to the product of the object's mass and the acceleration of gravity.

On Earth it is equal to 9.81 m/s^2, while on the moon it is equal to 1.62 m/s^2.

To provide a clear overview of all the variables influencing the material behavior and

the deposition dynamics, Table 3.1 summarizes the main parameters investigated in the simulations.

Parameter	Symbol	Description
Yield stress	τ_0	Minimum stress that causes the fluid to flow.
Shear modulus	G	Elastic resistance to transverse deformations.
Plastic viscosity	μ	Internal resistance of the fluid to flow.
Nozzle height	h_n	Distance from the printing surface.
Nozzle radius	r_n	Defines the filament size required for printing.
Printing velocity	v_p	The speed with which the nozzle moves.
Flow velocity	v_f	Extrusion speed of the material from the nozzle.
Gravity	g	Gravitational acceleration (Earth and Moon scenarios).

Table 3.1: Summary of the main parameters investigated in the simulations.

3.1.4. Geometric model and simulation setup

As a preliminary case study, a simple geometric model was used to form a reference to validate what can be done and has already been covered by other studies.

The geometric model chosen was a structure of three superimposed straight layers, each 15 cm long. During the various simulations the printed geometry remained the same in order to be able to consistently compare the various steps studied.

All the graphs that will be inserted will show the cross-sections taken halfway along the length of the printed geometry, therefore at 7.5 cm, to represent the average profile of the structure, as illustrated in Figure 3.2.

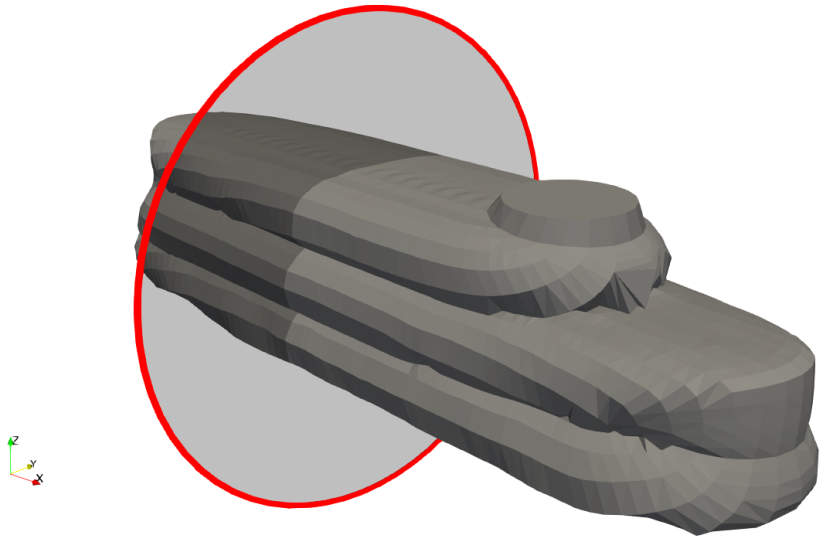

Figure 3.2: Average profile of the structure, represented by a cross-section taken halfway along the 15 cm printed geometry.

3.2. Influence of Yield Stress with Bingham Model

For the first tests, the Bingham fluid model was chosen, a model that is commonly adopted to reproduce the basic behavior of concrete in the fresh state [46].

Printable cementitious materials behave like visco-plastic Bingham materials. They flow only when subjected to stresses higher than a critical threshold value, the yield stress (τ_0) and when flowing, they show viscous behavior [52].

3.2.1. Analysis of Free Flow Deposition

The first phase of analysis started concerned simulations in free flow deposition printing mode, that is, the case in which the material is simply extruded and spreads by gravity. This allows us to focus on analyzing the effect of gravity without mechanical forcing.

To obtain a free flow deposition print the parameters to impose are the print parameters. In particular, equal printing and extrusion velocities of 0.1 m/s were chosen, to obtain a nominal process, and the equally chosen nozzle height and diameter of 2.5 cm in order to obtain a free-to-extrude filament.

With these settings, six simulations were performed and then compared with each other in the graphs that are reported later.

The parameters that were varied during this step are the gravity (g), terrestrial and lunar, a parameter that was varied in all steps of this thesis, and the yield stress (τ_0), of which the values 150, 300 and 600 Pa were taken, to evaluate how much pressure the pump must exert to move the material, that is, ensuring that the extruded mixture remains solid and with a shape necessary to support the subsequent layers.

The table below 3.2 indicates the other parameters chosen, kept the same for all simulations of this step.

Parameter	Value	Unit
Material Type	Bingham	–
Gravity (g)	9.81 – 1.62	m/s^2
Nozzle height (h_n)	0.025	m
Nozzle radius (r_n)	0.0125	m
Printing velocity (v_p)	0.1	m/s
Flow velocity (v_f)	-0.1	m/s
Yield Stress (τ_0)	150 – 300 – 600	Pa

Table 3.2: Summary table of physical and printing parameters - Bingham model - Free flow deposition.

3.2.1.1. Earth's gravity and comparison of different yield stress

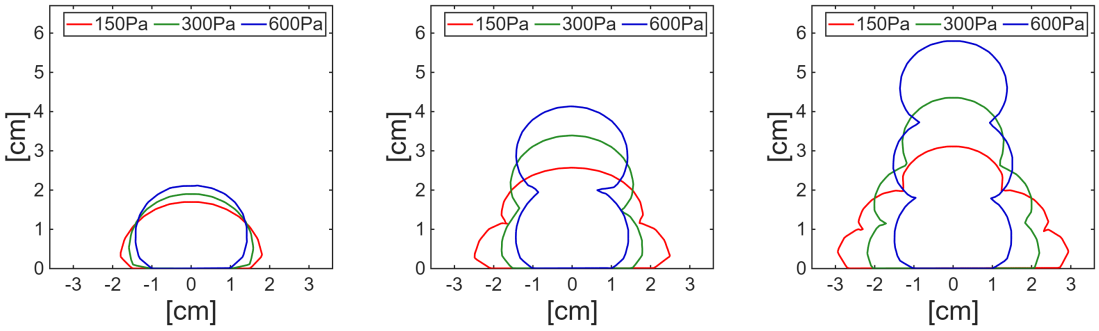

(a) First layer. (b) Two layers. (c) Three layers.

Figure 3.3: Earth's gravity - Printing in free flow deposition mode with the three yield stress values.

These first graphs with Earth's gravity show that as the yield stress decreases, the filaments tend to flatten and widen in the rigid plane. As a result, sections with lower yield values have larger widths and lower heights, while as the yield stress increases the layers take on

a more rounded and compact shape. Furthermore, it is observed that, as the number of layers increases (Figure 3.3c), the differences in height and width become more marked: with a yield stress of 150 Pa, the overlapping layers tend to lose compactness and expand more, a cumulative effect of weight, while in the case of a single layer (Figure 3.3a) the differences between the three yield values are much smaller.

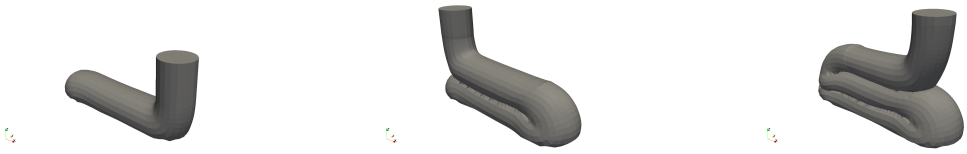

(a) First layer. (b) Two layers. (c) Three layers.

Figure 3.4: 3D image of printing - Free flow deposition - Earth's gravity - Example with yield stress value of 300 Pa.

3.2.1.2. Lunar gravity and comparison of different yield stress

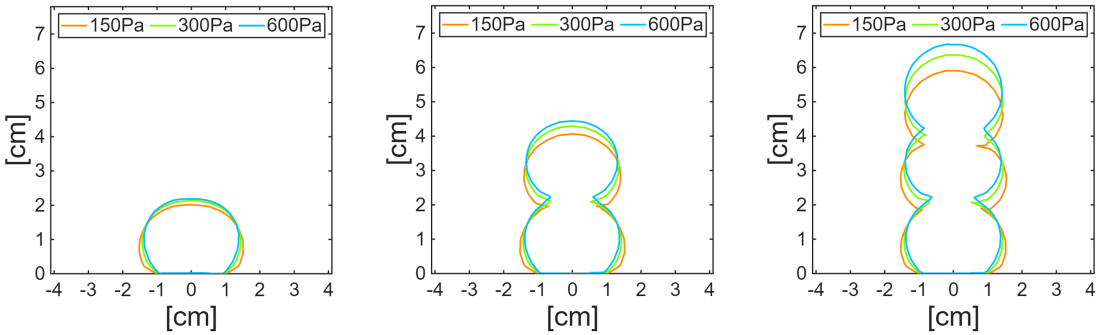

(a) First layer. (b) Two layers. (c) Three layers.

Figure 3.5: Lunar gravity - Printing in free flow deposition mode with the three yield stress values.

Graphs with lunar gravity show behavior similar to that observed for Earth's gravity. Again, as the yield stress decreases, the filaments tend to widen in the rigid plane; however, this effect is significantly attenuated. The three simulations with yield values of 150, 300

and 600 Pa show negligible differences between them, while maintaining the same trend observed in terrestrial conditions.

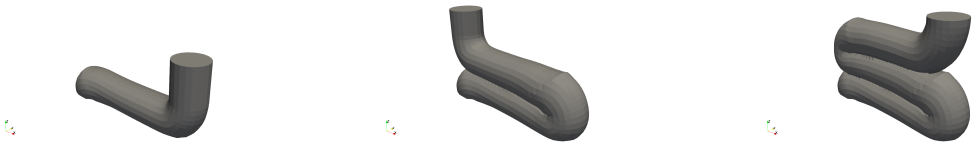

(a) First layer. (b) Two layers. (c) Three layers.

Figure 3.6: 3D image of printing - Free flow deposition - Lunar gravity - Example with yield stress value of 300 Pa.

3.2.1.3. Comparison of Earth's and lunar gravity, with the same yield stress

To directly compare the results obtained under the two gravitational conditions, comparative graphs were created comparing the cross-sections of filaments printed on Earth and the Moon for the same yield stress values.

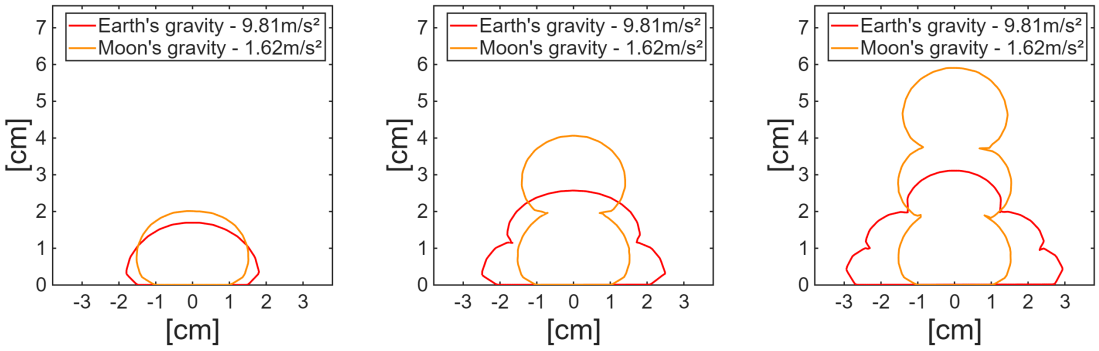

(a) First layer. (b) Two layers. (c) Three layers.

Figure 3.7: Free flow deposition - Comparison between printing under lunar gravity and Earth's gravity with yield stress of 150 Pa.

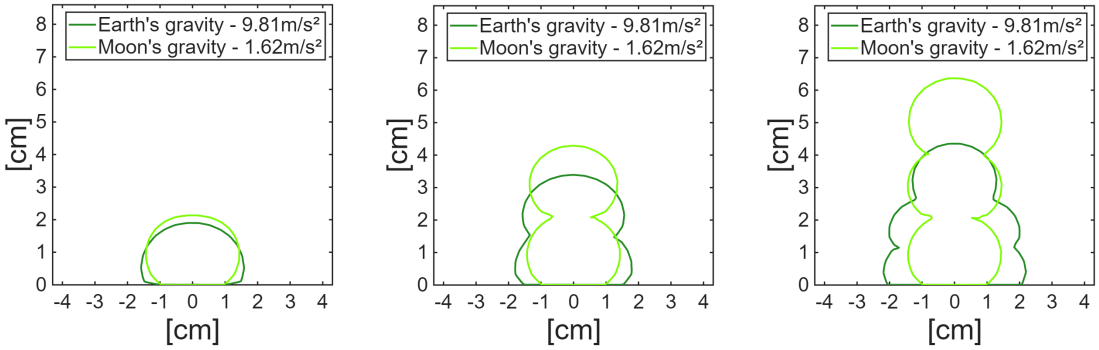

(a) First layer. (b) Two layers. (c) Three layers.

Figure 3.8: Free flow deposition - Comparison between printing under lunar gravity and Earth's gravity with yield stress of 300 Pa.

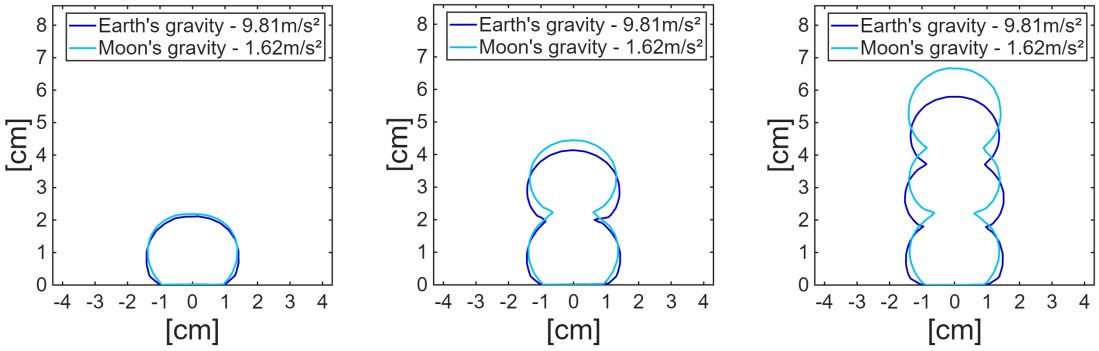

(a) First layer. (b) Two layers. (c) Three layers.

Figure 3.9: Free flow deposition - Comparison between printing under lunar gravity and Earth's gravity with yield stress of 600 Pa.

Simulation analysis shows that, under conditions of reduced gravity, filaments tend to take on a more rounded and compact shape than those printed in a terrestrial environment. Furthermore, the difference between the two environments is particularly evident for low yield values. In particular, at a yield stress of 150 Pa (Figure 3.7), the filament in lunar gravity is approximately twice as high and has a width half that printed in Earth's gravity. In contrast with a yield value of 600 Pa (Figure 3.9), the differences in height and width between the two conditions are significantly reduced. It can be observed how the lunar gravity favors maintaining the shape of the extruded material and even though the necessary pressure that the pump must exert to make the mixture flow is lower.

3.2.2. Analysis of Layer Pressing

A second set of analysis has been perfomed considering layer pressing printing mode, in which each layer is partially compressed or compacted by the next one and by the nozzle itself.

Compared to the free-flow deposition printing mode, this printing mode allows for better control of variables that are not considered in the first mode, which is assumed to be ideal. These variables include boundary conditions, the friction of the printing surface, and the friction between the robotic components of the printer, all of which can influence the printing conditions.

Geometry is set by varying the printing parameters. The nozzle height is set $h_n = 0,5 \cdot \phi_n$, and the printing velocity $v_p = 0,75 \cdot v_f$. With these values, the extruded filament undergoes compression that generates a pressure favorable to cohesion between the layers, unlike free-flow deposition tests, where the material was freely expanding and the printed filament was rounded in shape.

Under these conditions it will be possible to observe that the jet flattens and expands in the plane due to the lower height of the nozzle. Furthermore, the reduction in printing speed leads to an increase in the volume of material deposited per unit length, resulting in accumulation, crushing and greater filament width. By printing more slowly, the newly laid layer exerts more significant pressure on the previous one, thus improving fusion and cohesion between the layers.

Also in this mode, six simulations were performed and then compared with each other in the graphs that are reported subsequently.

The parameters that were varied during this step are gravity (g) and yield stress (τ_0).

The table below 3.3 indicates the other parameters chosen, kept the same for all simulations of this step.

Parameter	Value	Unit
Material Type	Bingham	–
Gravity (g)	9.81 – 1.62	m/s^2
Nozzle height (h_n)	0.0125	m
Nozzle radius (r_n)	0.0125	m
Printing velocity (v_p)	0.075	m/s
Flow velocity (v_f)	-0.1	m/s
Yield Stress (τ_0)	150 – 300 – 600	Pa

Table 3.3: Summary table of physical and printing parameters - Bingham model - Layer pressing.

3.2.2.1. Earth's gravity and comparison of different yield stress

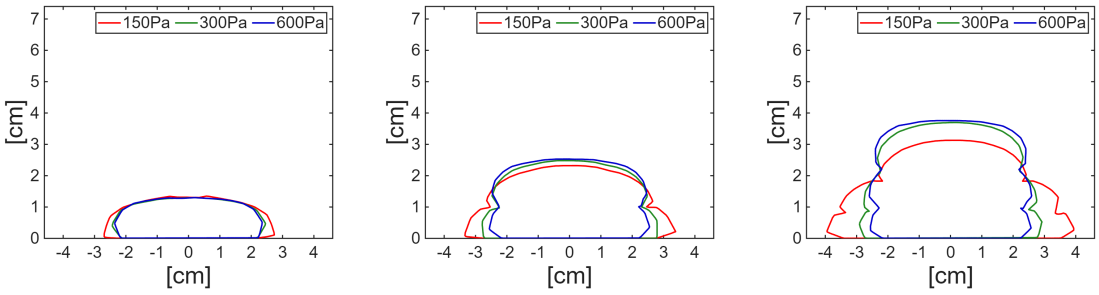

(a) First layer. (b) Two layers. (c) Three layers.

Figure 3.10: Earth's gravity - Printing in layer pressing mode with the three yield stress values.

The results of these simulations show that, under layer-pressing conditions, the first layer is similar for all yield strength values due to the compression applied by the nozzle. As the number of layers increases, and hence the pressure exerted between them, the differences become more apparent.

In particular, for a yield value of 150 Pa (Figure 3.10a), the filament appears considerably more flattened and widened in the plane, with a pyramidal shape: the first layer is much wider, due to the compression of the upper layers, than the third layer, located at the top. In contrast, for the values of 300 and 600 Pa (Figures 3.10band 3.10c), the geometry of the filaments remains almost unchanged and the overall deformation is smaller.

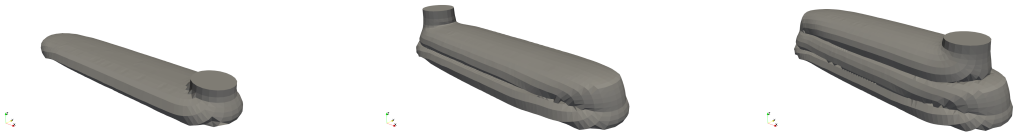

(a) First layer. (b) Two layers. (c) Three layers.

Figure 3.11: 3D image of printing - Layer pressing - Earth's gravity - Example with yield stress value of 300 Pa.

3.2.2.2. Lunar gravity and comparison of different yield stress

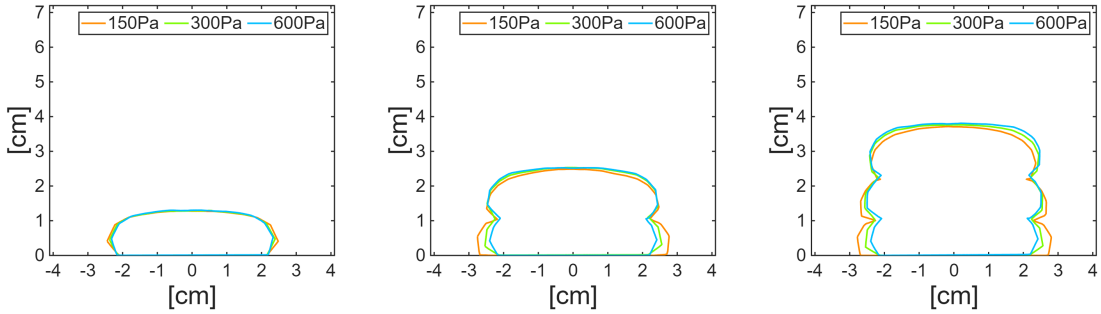

(a) First layer. (b) Two layers. (c) Three layers.

Figure 3.12: Lunar gravity - Printing in layer pressing mode with the three yield stress values.

These lunar gravity graphs are very similar to each other, with no significant differences in the shape of the filaments. In all simulations, however, a trend is observed that, as the number of layers increases, the width tends to increase due to the pressure exerted by the upper layers (progressive slump).

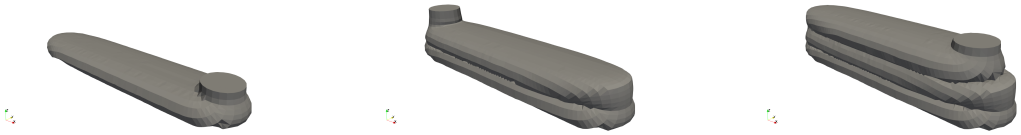

(a) First layer. (b) Two layers. (c) Three layers.

Figure 3.13: 3D image of printing - Layer pressing - Lunar gravity - Example with yield stress value of 300 Pa.

3.2.2.3. Comparison of Earth's and lunar gravity, with the same yield stress

Again, to directly compare the effects of gravity in the two environments, comparative graphs were made between the cross-sections of the filaments printed in terrestrial and lunar gravity, for each yield point value.

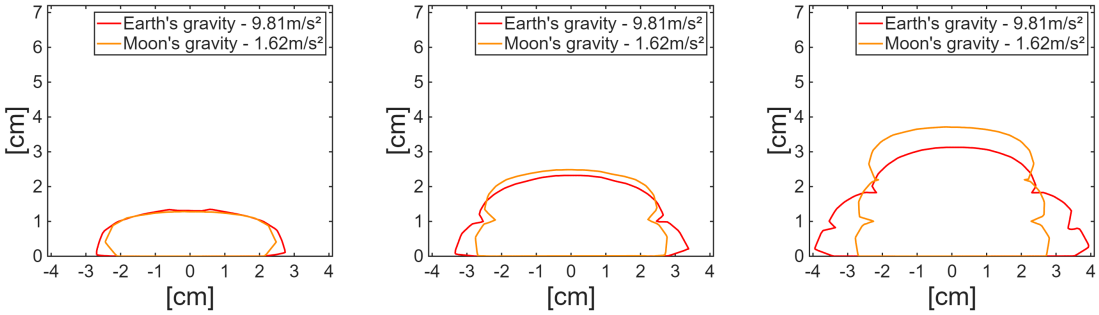

(a) First layer. (b) Two layers. (c) Three layers.

Figure 3.14: Layer pressing - Comparison between printing under lunar gravity and Earth's gravity with yield stress of 150 Pa.

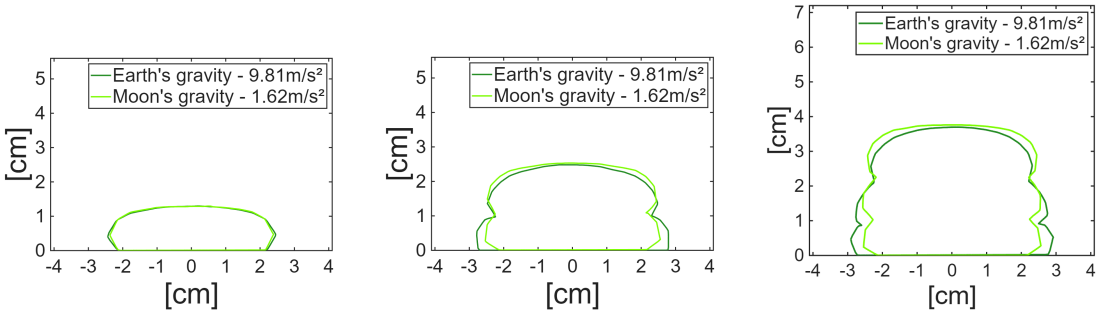

(a) First layer. (b) Two layers. (c) Three layers.

Figure 3.15: Layer pressing - Comparison between printing under lunar gravity and Earth's gravity with yield stress of 300 Pa.

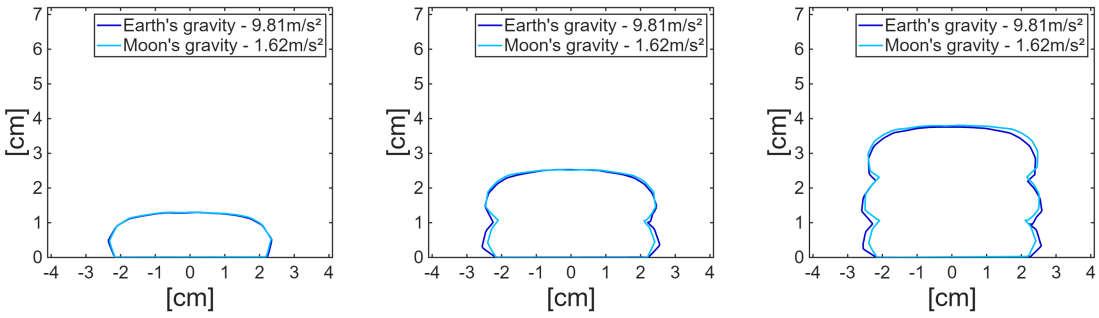

(a) First layer. (b) Two layers. (c) Three layers.

Figure 3.16: Layer pressing - Comparison between printing under lunar gravity and Earth's gravity with yield stress of 600 Pa.

From these comparisons it emerges that the layer-pressing condition significantly attenuates the influence of gravity. However, in the case of a yield strength of 150 Pa (Figure 3.14), the increase in the number of layers still highlights a difference: in Earth's gravity, a greater crushing of the layers is observed, which leads to a more pronounced expansion on the plane. For the higher yield values (300 and 600 Pa), however, the filament sections show a very similar shape in both conditions, in particular for the case with 600 Pa (Figure 3.16), where the effects of gravity are almost negligible.

Looking at the graphs resulting from all the simulations performed up to this point and reading what has been reported in the literature [50], it can be stated that the ratio between the extrusion speed and the printing speed constitutes one of the main parameters controlling the shape of the deposited filament.

3.3. Influence of Visco-Elasto-Plastic Behavior

For the second step, the fluid model was modified. While the Bingham model was used for the initial simulations, the elasto-viscoplastic (EVP) model was adopted for this stage, as it accounts for the elastic component of the material behavior. In fact, with the first model, a material is obtained that flows above the yield stress value cannot store elastic energy, therefore it cannot recover, deform or vibrate and then recover. While with this second type of model the filament deforms elastically under the load of the subsequent layers.

Physically, this means that the extruded mixture elastically resists immediate loads, such as the weight of successive layers, nozzle vibrations, and oscillations due to gravity; it deforms reversibly, until it reaches the yield stress and then flows as in the viscoplastic model.

Therefore in this second model the total deformation is formed by the viscoplastic part and the elastic part. This last part is governed by the shear modulus (G), a variable which for this second step has been varied and set at 30000 Pa.

The shear modulus represents the stiffness of the fresh material before it begins to flow.

3.3.1. Analysis of Free Flow Deposition

Simulations in free flow deposition printing mode were also initially performed in this step.

Six simulations were made and then compared with each other in the graphs which are reported subsequently.

Again the parameters that were varied during this step are gravity (g) and yield stress (τ_0), setting the chosen value of shear modulus at 30000 Pa.

The table below 3.4 indicates the other parameters chosen, kept the same for all simulations in this section.

Parameter	Value	Unit
Material Type	Viscoelastoplastic	–
Gravity (g)	9.81 – 1.62	m/s^2
Nozzle height (h_n)	0.025	m
Nozzle radius (r_n)	0.0125	m
Printing velocity (v_p)	0.1	m/s
Flow velocity (v_f)	-0.1	m/s
Yield Stress (τ_0)	150 – 300 – 600	Pa
Shear modulus (G)	30000	Pa

Table 3.4: Summary table of physical and printing parameters - Viscoelastoplastic model - Free flow deposition.

3.3.1.1. Earth's gravity and comparison of different yield stress

To analyze the difference between modeling with viscoplastic fluid and elastoviscoplastic fluid, it was chosen to make comparative graphs for each yield stress value separately, comparing it with the simulations performed during the previous step.

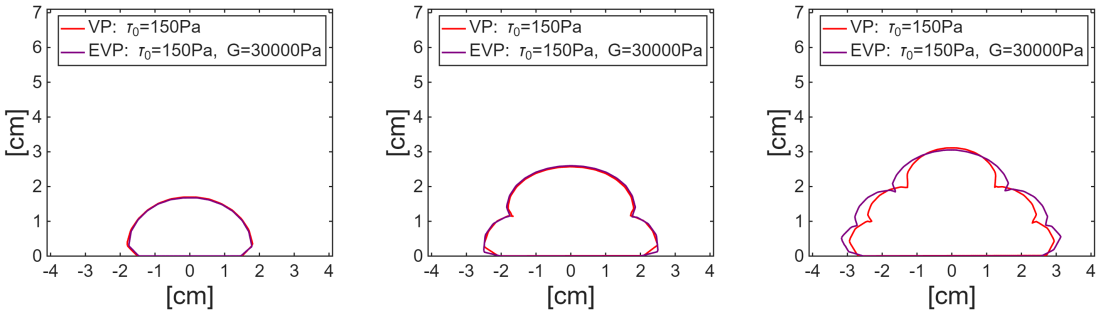

(a) First layer. (b) Two layers. (c) Three layers.

Figure 3.17: Free flow deposition - Comparison between printing VP and EVP fluid under Earth's gravity with yield stress of 150 Pa.

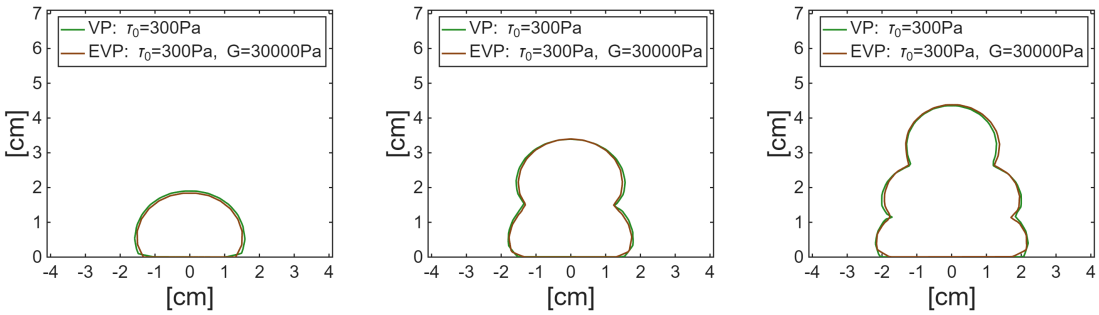

(a) First layer. (b) Two layers. (c) Three layers.

Figure 3.18: Free flow deposition - Comparison between printing VP and EVP fluid under Earth's gravity with yield stress of 300 Pa.

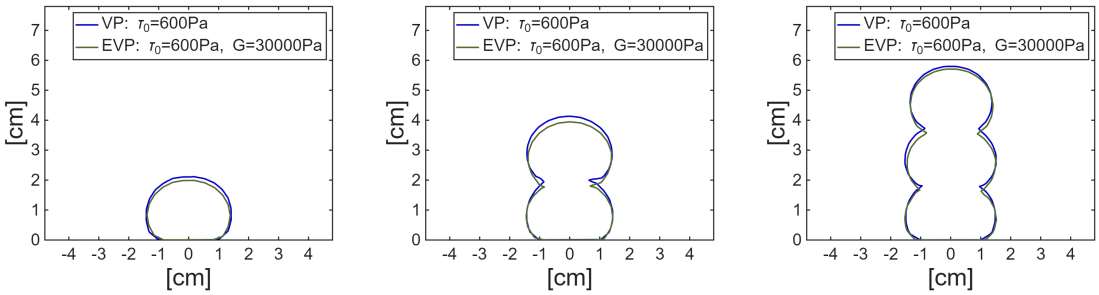

(a) First layer. (b) Two layers. (c) Three layers.

Figure 3.19: Free flow deposition - Comparison between printing VP and EVP fluid under Earth's gravity with yield stress of 600 Pa.

In these graphs it can be noted that in general the simulations of the two different models are similar, but there is a general tendency for elastoviscoplastic models to be more flattened than viscoplastic ones especially in the first layers, while at the end of printing the EVP simulations are no longer flattened. This is due to elastic memory, in fact the fluid has the ability to deform reversibly, therefore it can then recover its shape.

Furthermore, it can be noted that as yield stress increases, the difference between the two models becomes larger. This is due to the fact that the yield stress is lower, making the material smoother and more deformable; therefore, thanks to the elastic memory, once printed, it regains its shape more easily.

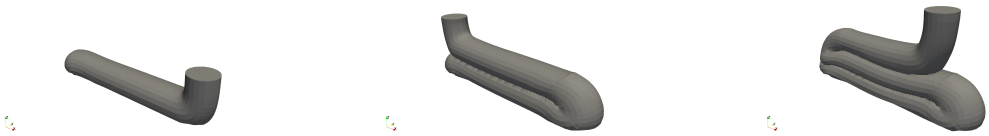

(a) First layer. (b) Two layers. (c) Three layers.

Figure 3.20: 3D image of printing - Elasto-Visco-Plastic model - Free flow deposition - Earth's gravity - Example with yield stress value of 300 Pa.

3.3.1.2. Lunar gravity and comparison of different yield stress

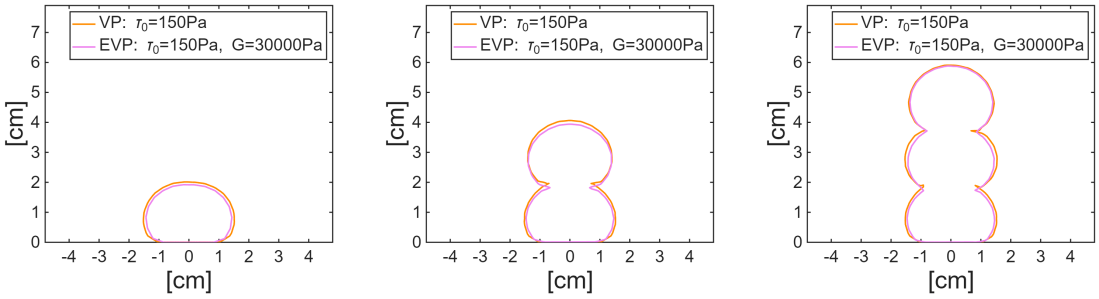

(a) First layer. (b) Two layers. (c) Three layers.

Figure 3.21: Free flow deposition - Comparison between printing VP and EVP fluid under Lunar gravity with yield stress of 150 Pa.

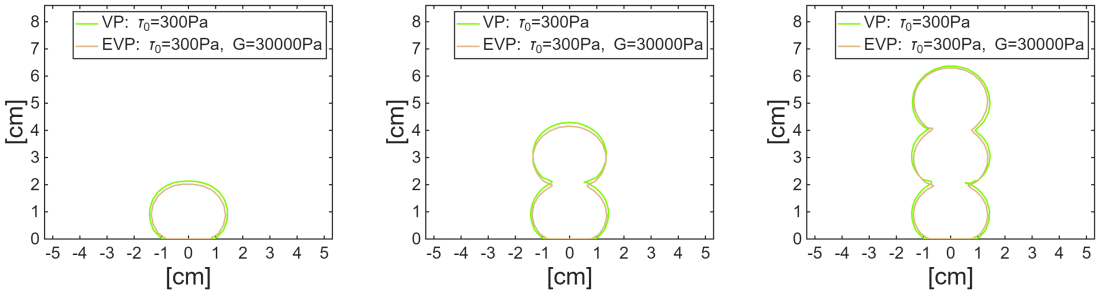

(a) First layer. (b) Two layers. (c) Three layers.

Figure 3.22: Free flow deposition - Comparison between printing VP and EVP fluid under Lunar gravity with yield stress of 300 Pa.

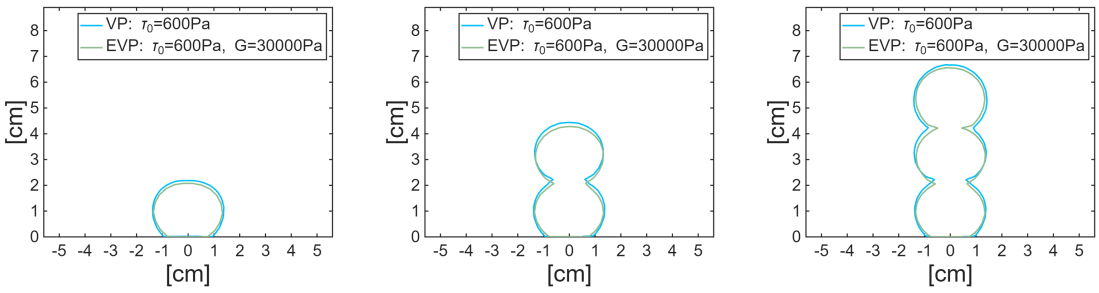

(a) First layer. (b) Two layers. (c) Three layers.

Figure 3.23: Free flow deposition - Comparison between printing VP and EVP fluid under Lunar gravity with yield stress of 600 Pa.

Even in the case of lunar gravity, the tendency of the EVP model to be more flattened is present, however the difference between the different yield stress values is similar between them. This is thanks to gravity, which, being lower, will have less of an effect on the extruded material; therefore, it is crushed less and must recover less, and in fact all the layers remain more rounded.

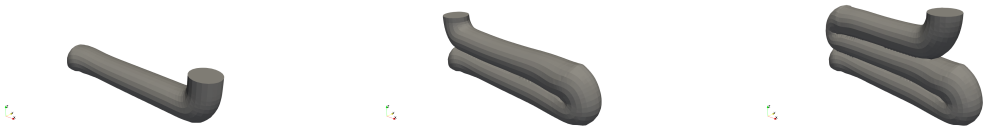

(a) First layer. (b) Two layers. (c) Three layers.

Figure 3.24: 3D image of printing - Elasto-Visco-Plastic model - Free flow deposition - Lunar gravity - Example with yield stress value of 300 Pa.

3.3.2. Analysis of Layer Pressing

Subsequently, simulations were performed with layer pressing printing modes.

The table below 3.5 indicates the other parameters chosen, kept the same for all simulations in this section.

Parameter	Value	Unit
Material Type	Viscoelastoplastic	–
Gravity (g)	9.81 – 1.62	m/s^2
Nozzle height (h_n)	0.0125	m
Nozzle radius (r_n)	0.0125	m
Printing velocity (v_p)	0.075	m/s
Flow velocity (v_f)	-0.1	m/s
Yield Stress (τ_0)	150 – 300 – 600	Pa
Shear modulus (G)	30000	Pa

Table 3.5: Summary table of physical and printing parameters - Viscoelastoplastic model - Layer pressing.

3.3.2.1. Earth's gravity and comparison of different yield stress

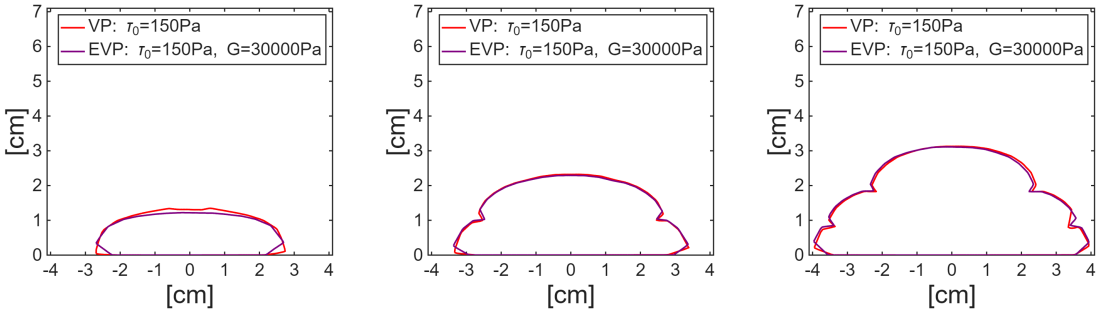

(a) First layer. (b) Two layers. (c) Three layers.

Figure 3.25: Layer pressing - Comparison between printing VP and EVP fluid under Earth's gravity with yield stress of 150 Pa.

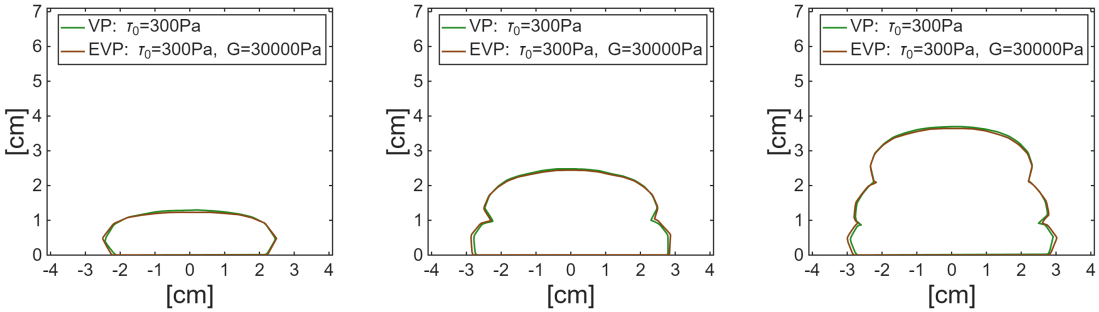

(a) First layer. (b) Two layers. (c) Three layers.

Figure 3.26: Layer pressing - Comparison between printing VP and EVP fluid under Earth's gravity with yield stress of 300 Pa.

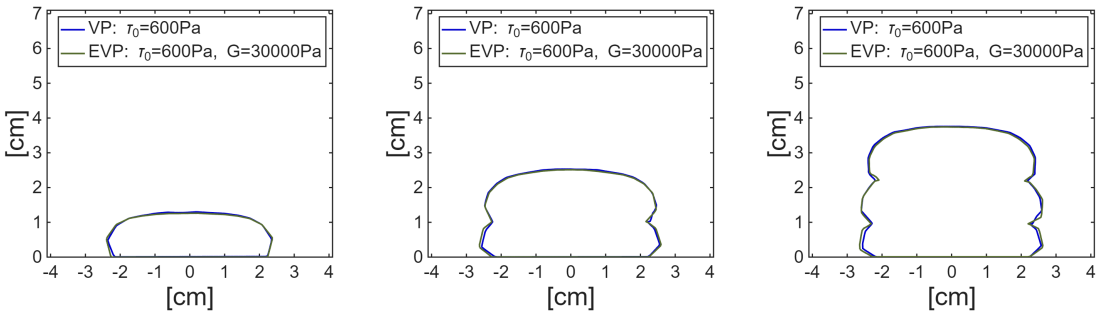

(a) First layer. (b) Two layers. (c) Three layers.

Figure 3.27: Layer pressing - Comparison between printing VP and EVP fluid under Earth's gravity with yield stress of 600 Pa.

In these graphs the two fluid models are very similar to each other, with the same tendency as the EVP model to be more deformed. In this case the smallest difference between the two types of simulations is due to the layer pressing printing mode, because the height of the nozzle compresses all the layers mechanically, without the possibility that the filament is free to take its shape, therefore the effect of elasticity is less.

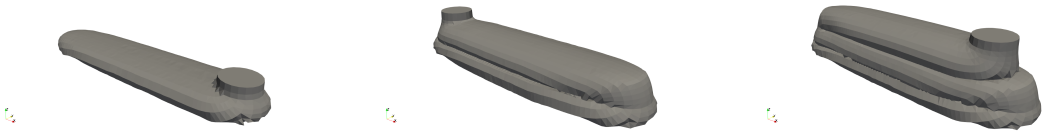

(a) First layer. (b) Two layers. (c) Three layers.

Figure 3.28: 3D image of printing - Elasto-Visco-Plastic model - Layer pressing - Earth's gravity - Example with yield stress value of 300 Pa.

3.3.2.2. Lunar gravity and comparison of different yield stress

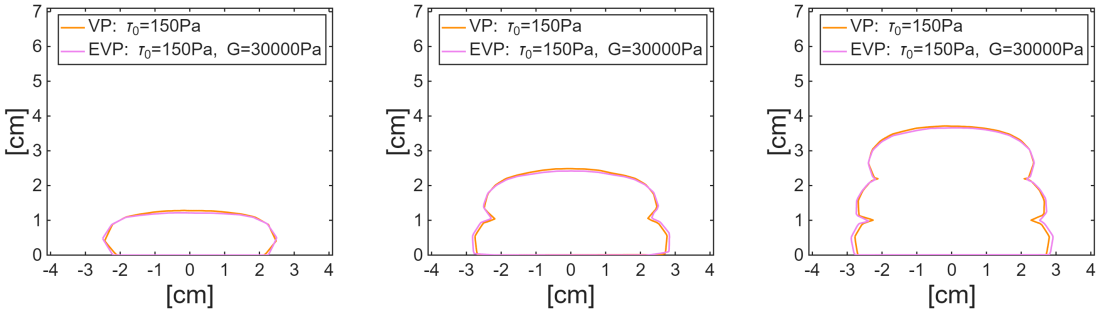

(a) First layer. (b) Two layers. (c) Three layers.

Figure 3.29: Layer pressing - Comparison between printing VP and EVP fluid under Lunar gravity with yield stress of 150 Pa.

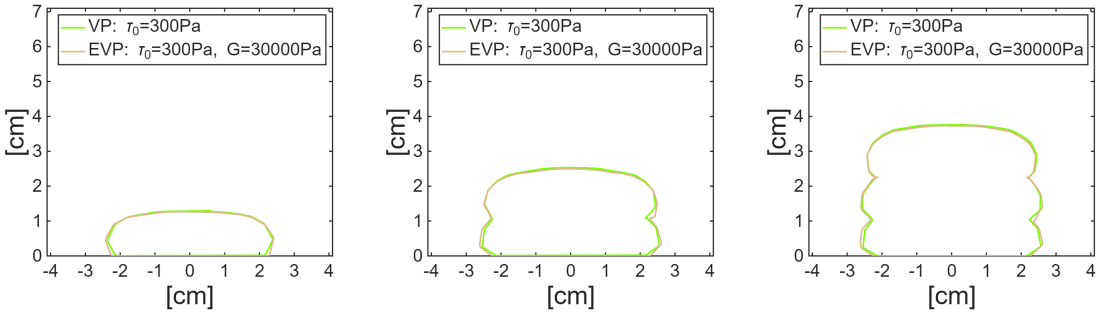

(a) First layer. (b) Two layers. (c) Three layers.

Figure 3.30: Layer pressing - Comparison between printing VP and EVP fluid under Lunar gravity with yield stress of 300 Pa.

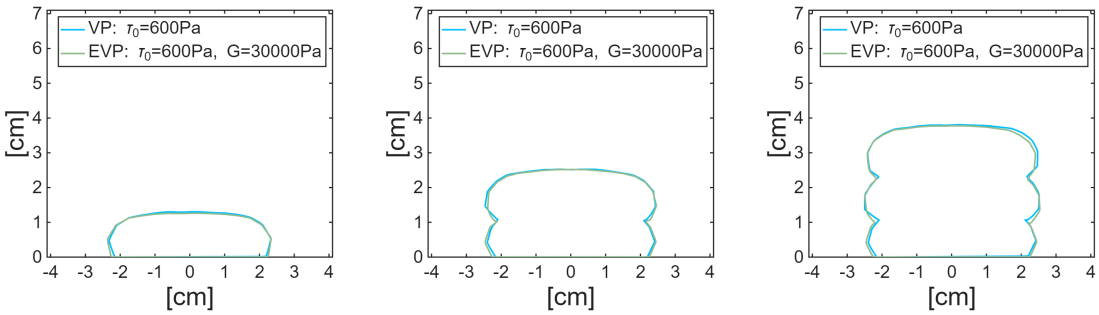

(a) First layer. (b) Two layers. (c) Three layers.

Figure 3.31: Layer pressing - Comparison between printing VP and EVP fluid under Lunar gravity with yield stress of 600 Pa.

These lunar gravity simulations are very similar to previous Earth's gravity simulations. The difference that can be noted is that the layers are still more rounded thanks to the lesser effect of gravity, however due to the printing mode the simulations with the two fluid models are very similar to each other.

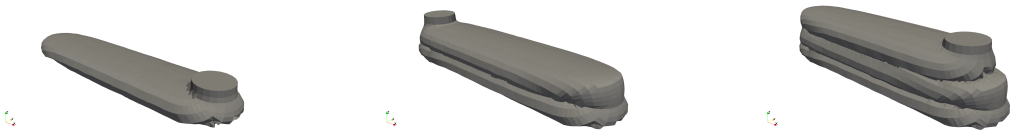

(a) First layer. (b) Two layers. (c) Three layers.

Figure 3.32: 3D image of printing - Elasto-Visco-Plastic model - Layer pressing - Lunar gravity - Example with yield stress value of 300 Pa.

3.4. Influence of Shear Modulus

The next step was to investigate the effect of shear modulus (G). To do this, it was chosen to set the yield stress value at 600 Pa, this is because, as shown in the previous steps, it helps to evaluate the geometric definition of the extruded filament, which remains defined and formed after printing.

For the same yield stress, the material may not collapse, therefore not exceed the yield stress value, but deform too elastically and therefore remain too crushed or unstable. In fact, a low G value determines a softer material, while with a high G value the material will be more rigid.

For 3d printing, where each filament must carry the weight of the upper filaments immediately, a higher shear modulus is required than in fresh concrete used for classical construction, which does not require the stiffness to carry more material on top.

In this step, eight simulations were performed and then compared with each other in the graphs which are then reported with the simulations performed in the previous step.

3.4.1. Analysis of Free Flow Deposition

The first simulations were performed under free flow deposition printing conditions.

The parameters that were varied during this step are the gravity (g), terrestrial and lunar, a parameter that was varied in all steps of this thesis, and the shear modulus (G), of which the values 10000, 20000 and 30000 Pa were taken, to evaluate how much the stiffness influences the final quality of the print.

The table below 3.6 indicates the other parameters chosen, kept the same for all simulations in this section.

Parameter	Value	Unit
Material Type	Viscoelastoplastic	–
Gravity (g)	9.81 – 1.62	m/s^2
Nozzle height (h_n)	0.025	m
Nozzle radius (r_n)	0.0125	m
Printing velocity (v_p)	0.1	m/s
Flow velocity (v_f)	-0.1	m/s
Yield Stress (τ_0)	600	Pa
Shear modulus (G)	10000 – 20000 – 30000	Pa

Table 3.6: Summary table of physical and printing parameters - Viscoelastoplastic model - Free flow deposition.

3.4.1.1. Earth's gravity and comparison of different shear modulus

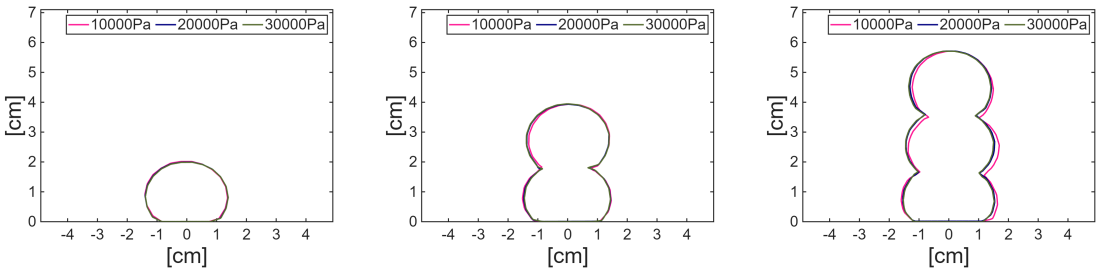

(a) First layer. (b) Two layers. (c) Three layers.

Figure 3.33: Earth's gravity - Printing in free flow deposition mode with the three shear modulus values.

In these graphs it is found that the Earth's gravity simulations are similar to each other, with a greater discrepancy for the smaller value of shear modulus. The print with the 10000 Pa shear modulus is more flattened than the other two models, which are almost

overlapped and difficult to distinguish.

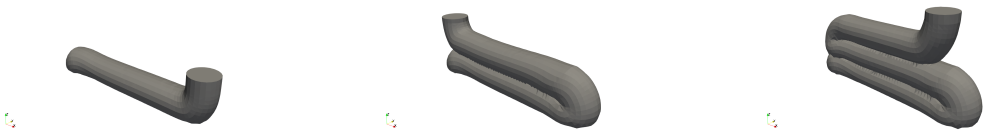

(a) First layer. (b) Two layers. (c) Three layers.

Figure 3.34: 3D image of printing - Elasto-Visco-Plastic model - Free flow deposition - Earth's gravity - Example with shear modulus of 20000 Pa.

3.4.1.2. Lunar gravity and comparison of different shear modulus

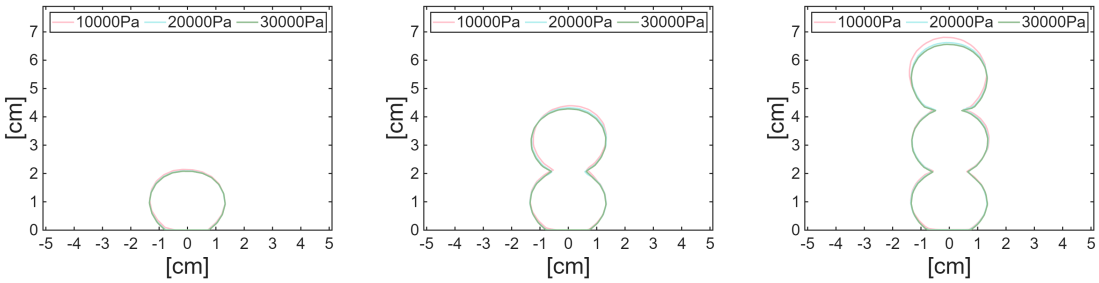

(a) First layer. (b) Two layers. (c) Three layers.

Figure 3.35: Lunar gravity - Printing in free flow deposition mode with the three shear modulus values.

With lunar gravity, the difference with the case of a smaller shear modulus is also not found; therefore, all three simulations are similar to each other. This is due to the reduced self-weight, thanks to the lunar gravity, which being smaller does not deform the extruded filaments, therefore even with a smaller G, the effect of softer material is less.

(a) First layer. (b) Two layers. (c) Three layers.

Figure 3.36: 3D image of printing - Elasto-Visco-Plastic model - Free flow deposition - Lunar gravity - Example with shear modulus of 20000 Pa.

3.4.2. Analysis of Layer Pressing

Simulations were then performed under layer pressing printing conditions.

The table below 3.7 indicates the other parameters chosen, kept the same for all simulations in this section.

Parameter	Value	Unit
Material Type	Viscoelastoplastic	–
Gravity (g)	9.81 – 1.62	m/s^2
Nozzle height (h_n)	0.0125	m
Nozzle radius (r_n)	0.0125	m
Printing velocity (v_p)	0.075	m/s
Flow velocity (v_f)	-0.1	m/s
Yield Stress (τ_0)	600	Pa
Shear modulus (G)	10000 – 20000 – 30000	Pa

Table 3.7: Summary table of physical and printing parameters - Viscoelastoplastic model - Layer pressing.

3.4.2.1. Earth's gravity and comparison of different shear modulus

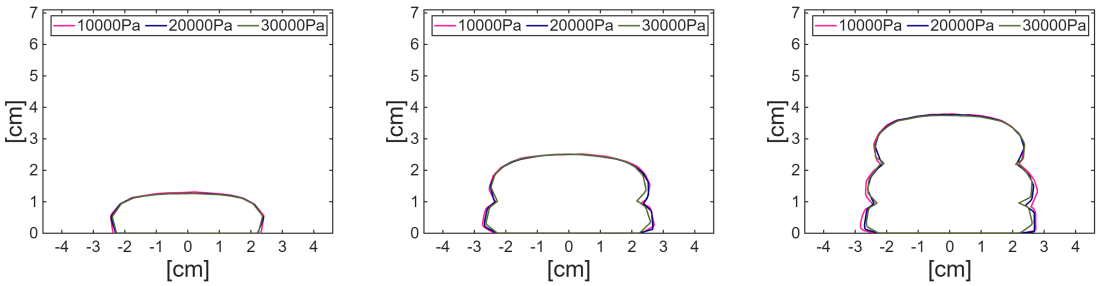

(a) First layer. (b) Two layers. (c) Three layers.

Figure 3.37: Earth's gravity - Printing in layer printing mode with the three shear modulus values.

The results still show that under layer pressing conditions, since there is a mechanical influence due to the movement of the nozzle, the difference between the simulations is smaller. The only difference that can be noticed is that the model with the lowest shear modulus shows a failure compared to the other models.

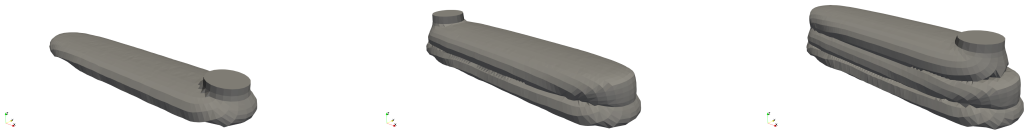

(a) First layer. (b) Two layers. (c) Three layers.

Figure 3.38: 3D image of printing - Elasto-Visco-Plastic model - Layer pressing - Earth's gravity - Example with shear modulus of 20000 Pa.

3.4.2.2. Lunar gravity and comparison of different shear modulus

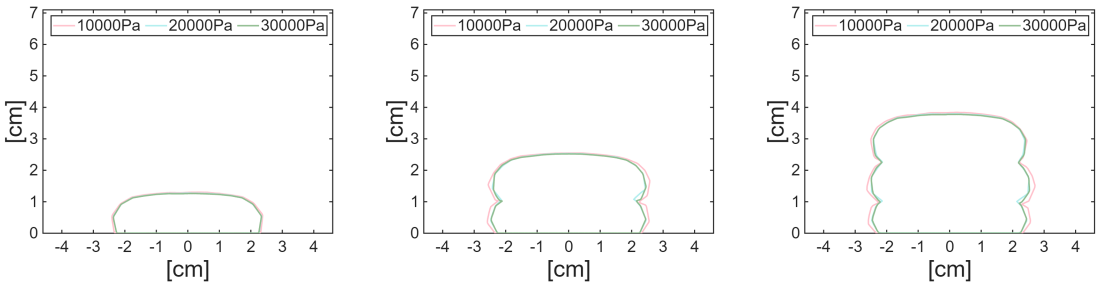

(a) First layer. (b) Two layers. (c) Three layers.

Figure 3.39: Lunar gravity - Printing in layer printing mode with the three shear modulus values.

Even with lunar gravity the trend of the layer pressing effect is the same as with Earth's gravity. And just like the previous simulations, the model with the smaller shear modulus is softer than the other two models.

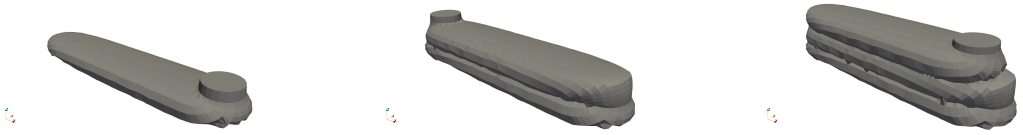

(a) First layer. (b) Two layers. (c) Three layers.

Figure 3.40: 3D image of printing - Elasto-Visco-Plastic model - Layer pressing - Lunar gravity - Example with shear modulus of 20000 Pa.

4 | Effect of gravity on buildability

The final phase of this project consisted in printing a 15 cm wall inclined by 10° with respect to the vertical, until its collapse.

Until now, the printability of the material under the various proposed conditions has been mainly verified. With these latest simulations the aim is instead to examine the buildability of the printing process.

Therefore, the aim is to analyze the global and structural level of the print, while in previous phases it had been studied at a local level, the 3 layers served to understand the shape of the filaments and the interaction between them.

The sloping wall was modeled with a multi-level toolpath ensuring that the print continued until it collapsed, without stopping before the end of the geometry.

The values varied in this step were only the printing mode and the gravity, while the value fixed on the basis of the previous tests was the chosen yield stress equal to 1000 Pa.

These high values were taken because being an inclined geometry and with 3D printing it is necessary to have stability and for the fluid high stiffness is required once extruded.

4.1. Free flow deposition

The first two cases are in free flow deposition print conditions.

The table below 4.1 indicates the chosen parameters, kept the same for all simulations in this section.

Parameter	Value	Unit
Material Type	Bingham	–
Gravity (g)	9.81 – 1.62	m/s^2
Nozzle height (h_n)	0.025	m
Nozzle radius (r_n)	0.0125	m
Printing velocity (v_p)	0.1	m/s
Flow velocity (v_f)	-0.1	m/s
Yield Stress (τ_0)	1000	Pa

Table 4.1: Summary table of physical and printing parameters - Buildability - Free flow deposition.

4.1.1. Earth's gravity

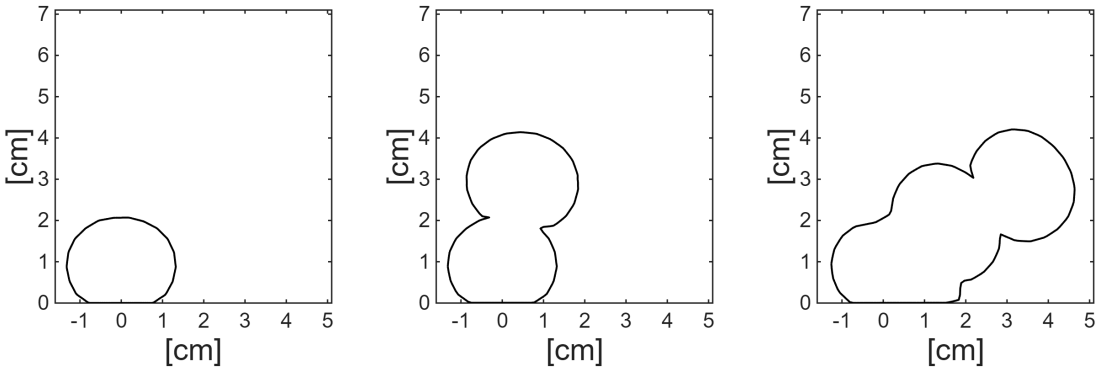

(a) First layer. (b) Two layers. (c) Collapse.

Figure 4.1: Wall printing under Earth's gravity and free flow deposition modality.

With Earth's gravity the wall collapsed during the printing of the third layer.

The collapse occurs suddenly during the printing of the third layer, as soon as the extruded filament touches the second layer the structure begins to fall during the length of the entire wall. Therefore global instability has caused the entire structure to overturn.

After studying the results obtained thus far, it can be deduced that this is the most unfavorable case for wall printing. This is because the filament is free to expand and gravity has a greater effect.

Thus the poor geometric cohesion, due to the circular section which leads to a small contact surface between the layers, and the high self-weight caused the geometry to collapse early.

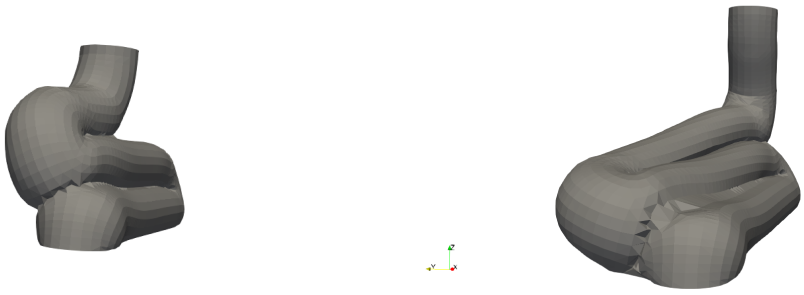

(a) Complete layers. (b) Collapse.

Figure 4.2: 3D image of wall printing under Earth's gravity and free flow deposition modality.

4.1.2. Lunar gravity

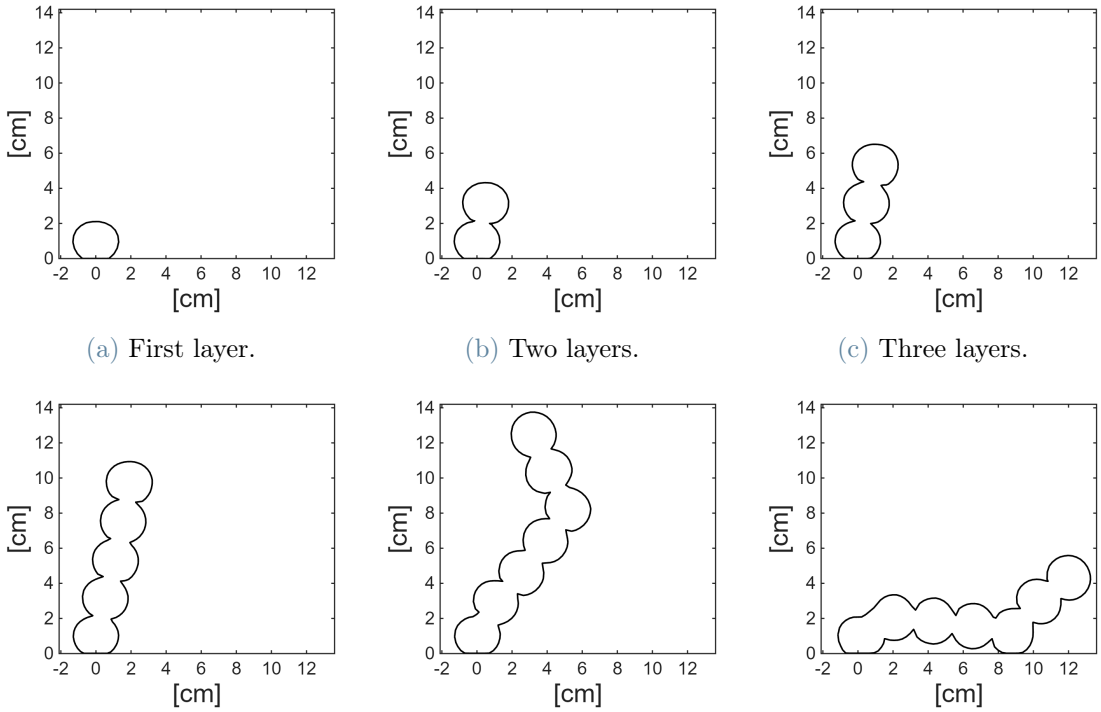

(a) First layer. (b) Two layers. (c) Three layers.

(d) Five layers. (e) Seven layers. (f) Collapse.

Figure 4.3: Wall printing under Lunar gravity and free flow deposition modality.

Compared to the previous test, in this simulation the effect of lunar gravity is explicitly seen: the wall begins to collapse during the printing of the sixth layer and finally collapses only after the seventh layer.

The graphs above show how the print is rounded and the layers are not well bonded to each other, due to the limited contact surface between them, but thanks to the reduced gravity the geometry remains intact for several levels.

In this case the collapse does not occur as clearly as in the previous case, but occurs after a deformation. In fact, after the first layer, the structure begins to bend, does not collapse due to reduced gravity, and only during the printing of the seventh layer does the wall collapse because excessive deformation takes the wall out of the nozzle's trajectory;

consequently, the nozzle deposits the material into the void, causing the entire structure to fall.

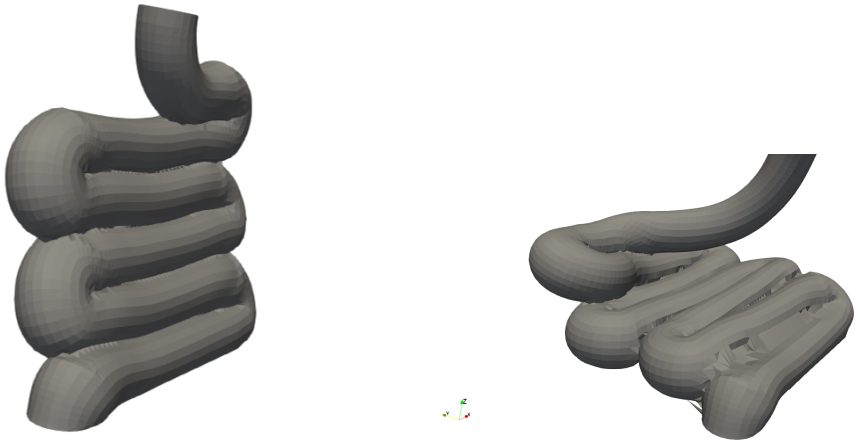

(a) Complete layers. (b) Collapse.

Figure 4.4: 3D image of wall printing under Lunar gravity and free flow deposition modality.

4.2. Layer pressing

The last two cases are in layer pressing printing conditions. As previously defined, in this mode the material is not free to expand, but each layer is partially compressed and compacted by the nozzle during the extrusion process.

The table below 4.2 indicates the chosen parameters, kept the same for all simulations in this section.

Parameter	Value	Unit
Material Type	Bingham	–
Gravity (g)	9.81 – 1.62	m/s^2
Nozzle height (h_n)	0.0125	m
Nozzle radius (r_n)	0.0125	m
Printing velocity (v_p)	0.075	m/s
Flow velocity (v_f)	-0.1	m/s
Yield Stress (τ_0)	1000	Pa

Table 4.2: Summary table of physical and printing parameters - Buildability - Layer pressing.

4.2.1. Earth's gravity

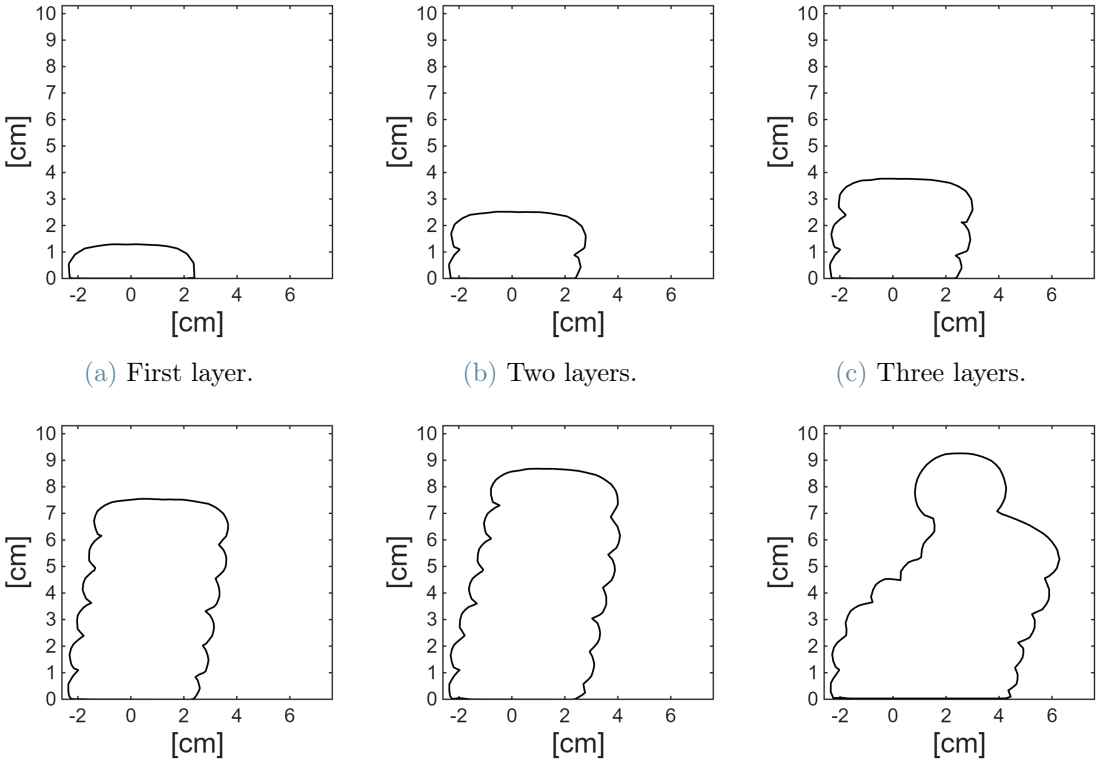

(a) First layer. (b) Two layers. (c) Three layers.

(d) Six layers. (e) Seven layers. (f) Collapse.

Figure 4.5: Wall printing under Earth's gravity and layer pressing modality.

Under layer pressing conditions with Earth's gravity, the stability of the print is significantly increased.

Compared to the first case where the wall collapsed after the second layer, in this model the print reaches up to the seventh layer and collapses during the printing of the eighth.

In quantitative terms, more than triple the number of layers is reached and at the physical height level the structure doubles its height, going from just over 4 cm to almost 9 cm. This is due to the ability of the layer pressing condition to compact the layers by increasing the contact surface between them.

In this case, the collapse occurs as in the first simulation; therefore, during the printing

of the eighth layer, the wall gives way. However, unlike the two previous cases, where the failure occurred simultaneously with the deposition of the critical layer, in this case the instability initiates in the bottom layers. The progressive failure at the base ultimately triggers the overturning of the entire structure.

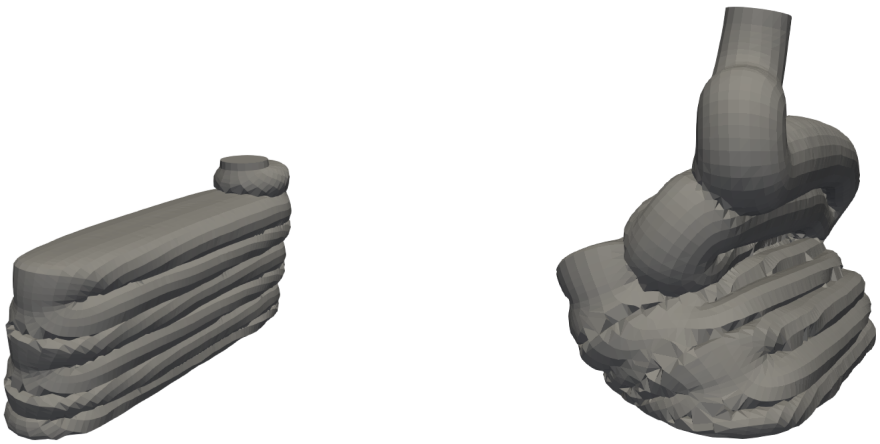

(a) Complete layers. (b) Collapse.

Figure 4.6: 3D image of wall printing under Earth's gravity and layer pressing modality.

4.2.2. Lunar gravity

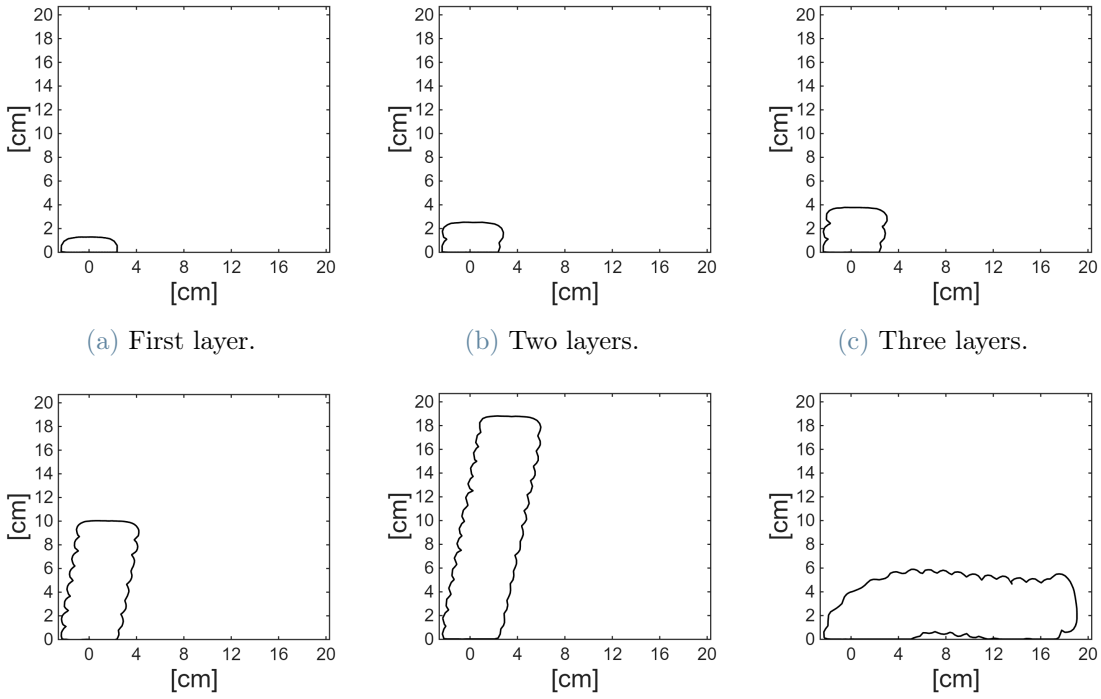

(a) First layer. (b) Two layers. (c) Three layers.

(d) Eight layers. (e) Fifteen layers. (f) Collapse.

Figure 4.7: Wall printing under Lunar gravity and layer pressing modality.

The last simulation performed is with lunar gravity and under layer pressing printing conditions.

This is the optimal case, in fact, it collapses after the fifteenth layer and reaches a height of approximately 19 cm. Compared to the previous case which reaches about 10 cm, both the height and the number of layers double.

This is because, while lower gravity reduces the static load by delaying collapse, the layer pressing condition ensures adhesion between the layers. This last aspect is very important, because reduced gravity alone would not exert sufficient pressure to join the layers, compacting the weak structure. The mechanical compression action of the nozzle compensates for this deficit.

In this case too, the collapse does not occur due to geometric misalignment, the printing of the layer with respect to the structure, as in cases with free flow deposition, but occurs due to the collapse of the underlying structure which leads to the collapse of the entire wall.

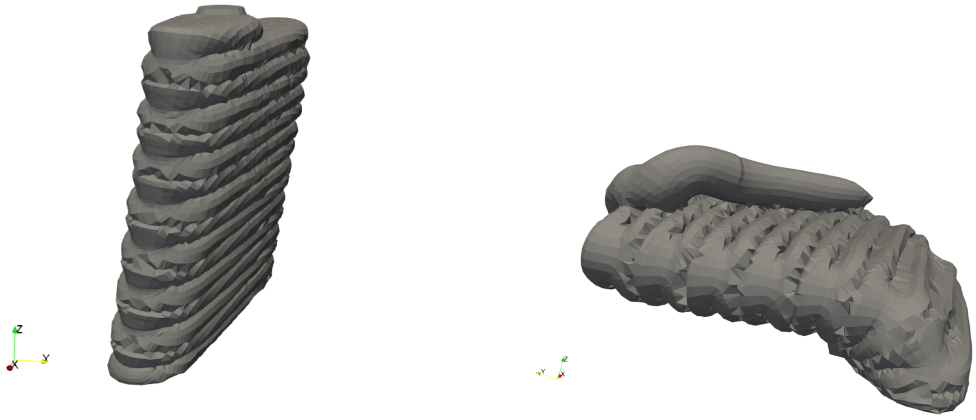

(a) Complete layers. (b) Collapse.

Figure 4.8: 3D image of wall printing under Lunar gravity and layer pressing modality.

4.3. Comparison of the tests performed

		N. layers	Height [cm]	Collapse
Free flow deposition	Earth's gravity	2	4	Immediate collapse
	Lunar gravity	5	11	Geometric misalignment
Layer pressing	Earth's gravity	7	9	Failure of the first layers
	Lunar gravity	15	19	Collapse of the entire structure

Table 4.3: Comparison of buildability results.

Observing the summary data presented in Table 4.3, a clear distinction emerges between terrestrial and lunar scenarios. The comparison between the two gravitational environments highlights how gravity is the dominant factor in determining the maximum number of printable layers before collapse. Specifically, while the number of layers stabilizes at very low values under Earth's gravity (between 3 and 6 layers), a drastic increase in printability is observed in lunar gravity, reaching up to 15 layers in the case of layer pressing.

Another significant finding from the table is the effectiveness of the layer pressing technique compared to free flow: across almost all steps and conditions, the application of pressure or layer compaction allows for greater heights, thanks to the resulting improvement in density and interlayer adhesion.

To correctly interpret these results, it is fundamental to address the concept of Buildability, which is defined as the ability of the fresh mixture to support its own weight and that of subsequent layers without excessive deformation or collapse [53] [54].

The phenomenon of collapse during 3D printing is generally described as a competition between two opposing forces: the increasing load, where the vertical pressure on the lower layers increases due to the weight of the overlying material as new layers are deposited, and the material resistance, as the material must simultaneously develop sufficient mechanical strength to counteract this load.

Structural failure typically occurs when the gravity-induced stress exceeds the yield stress of the material in the bottom layer [53] [55]. There are primarily two modes of failure, namely plastic collapse, where the material yields and is crushed, or elastic instability, where the wall bows or collapses laterally, a phenomenon known as buckling [55] [56].

The simulation results summarized in the table align perfectly with this theory. Lunar gravity, being one-sixth of Earth's, drastically reduces the "increasing load" generated by each new layer. Consequently, given equal rheological properties of the material, the stress on the lower layers remains below the critical threshold for much longer, allowing for the printing of significantly taller structures.

Furthermore, buildability is strongly influenced by the material's thixotropy, which refers to its ability to increase viscosity and structural strength when at rest [57]. After extrusion, the material must quickly recover its internal structure to support the subsequent layer. The use of layer pressing observed in the table appears to favor this mechanism: by compacting the material, voids are reduced and the immediate load-bearing capacity is increased, thereby delaying the moment of collapse compared to free flow deposition.

The data confirms that for in-situ applications on low-gravity celestial bodies, the rheological requirements for buildability are less stringent than on Earth, potentially allowing for the use of mixtures with lower yield stress or, conversely, the construction of more slender structures using the same materials.

5 | Conclusions and future developments

This thesis aims to investigate the applicability and potential of 3D Concrete Printing (3DCP) technology for the construction of infrastructure in extraterrestrial environments, with specific reference to the lunar context. The research stems from the need to understand how environmental conditions, and in particular a reduced gravity approximately one-sixth that of Earth, influence the deposition dynamics of the material, the shape of the filament, and the structural stability of the printed elements.

The methodological approach adopted for the development of the thesis relies on numerical simulations, an essential tool for predicting the behavior of fresh material and validating process parameters without the aid of a physical printer. Specifically, the analyses were conducted using the Particle Finite Element Method (PFEM) within a Lagrangian framework, a choice motivated by the ability of this method to effectively model free-surface flows and large deformations typical of the extrusion and deposition process.

To accurately describe the rheological behavior of cementitious mixtures, two different constitutive models were implemented: the Bingham model, used to represent the basic visco-plastic behavior of the material, and the Saramito model (Elasto-Visco-Plastic or EVP), which integrates the elastic component, enabling the evaluation of transitions between solid and fluid states.

Through extensive parametric analysis, the study examined the influence of key material variables, such as yield stress and shear modulus, systematically comparing free flow deposition and layer pressing modes in both terrestrial and lunar environments, in order to

determine their effects on filament geometry and overall structure buildability.

5.1. Main results

Numerical simulations conducted in this study provided quantitative evidence regarding the material behavior and structural stability of the printed elements, confirming the distinct advantages of the lunar environment over terrestrial conditions. The parametric analysis described in Chapter 4 revealed that gravity plays a decisive role in defining the geometry of the extruded filament. Under Earth's gravity, the material tends to flatten significantly due to its own weight, showing a marked slump effect, particularly when using mixtures with lower yield stress values. Conversely, in the lunar environment, reduced gravitational acceleration ($1.62\,m/s^2$) attenuates this phenomenon, allowing the filaments to maintain a more rounded and compact cross-section.

However, the introduction of the layer pressing technique has proven to be a dominant factor, capable of overriding these gravitational effects. By mechanically compressing the layers, this deposition mode not only reduces geometric discrepancies between terrestrial and lunar prints, but is also essential for increasing the contact surface and promoting interlayer adhesion, a critical aspect for structural integrity.

These results on filament geometry were further confirmed by the buildability tests reported in Chapter 5, where the combined effect of gravity and deposition mode on a wall printed until collapse was analyzed. The results identified gravity as the primary constraint on vertical growth: under Earth's gravity, the structure collapsed after a few layers due to rapidly increasing vertical stress. In contrast, the lunar context allowed for a substantial increase in buildability, with the structure reaching up to 15 layers in the optimal configuration.

Crucially, simulations have shown that while lunar gravity delays the onset of plastic collapse by reducing the vertical load, it is the synergy with layer pressing that ensures the best results. Consequently, the optimal printing scenario identified involves the use of layer pressing in a lunar environment, which allowed the structure to reach a height of

about 19 cm, more than double that obtained under terrestrial conditions.

5.2. Contribution and practical implications

From a scientific perspective, this thesis provides a robust numerical framework for predicting the behavior of fresh cementitious materials under reduced gravity conditions. Unlike existing literature, which often relies on ground-based experiments with simulants or simplified analytical models, this study utilizes the Particle Finite Element Method (PFEM) to decouple the effects of gravity from other process parameters. This approach has proven effective in managing the large deformations and free-surface flows typical of 3DCP, validating the reliability of the method for complex extraterrestrial scenarios where physical tests are currently unfeasible. A novel element lies in the comparative application of the constitutive Bingham and Saramito (EVP) models in the lunar context; the analysis highlighted that, although the Bingham model is sufficient to describe the macro-flow behavior and plastic collapse, the integration of the elastic component into the EVP model offers a more accurate representation of the shape maintenance and deformation history, especially in the first layers where elastic recovery plays an important role.

In terms of practical implications, the results obtained offer direct guidelines for the planning of future in situ additive manufacturing missions to the Moon. The adoption of the layer pressing technique is identified as a recommended standard for lunar printing, not merely for geometric correction, but primarily to promote adhesion between layers, compensating for the reduced gravitational settling that would otherwise lead to weak interfaces and porosity.

Furthermore, this evidence leads to a significant reconsideration of the rheological requirements, which prove to be significantly less stringent on the Moon than on Earth. The reduced gravitational acceleration in fact allows the use of materials with a lower yield stress (as observed in the 150 Pa simulations), which on Earth would be unprintable due to the immediate slump, but which maintain stability in the lunar environment. This suggests designing lunar mixtures, such as geopolymer-regolite composites, prioritizing pumpability and open time rather than immediate high stiffness. To maximize structural integrity,

it is essential to calibrate process parameters to induce the "pressing" effect, particularly by maintaining a nozzle height lower than its diameter and synchronizing the extrusion speed with the printing speed. In conclusion, the research suggests a paradigm shift for lunar 3DCP: the construction strategy should not rely exclusively on high-performance materials to counteract gravity, but rather focus on process-driven consolidation (layer pressing) applied to more workable materials, thus maximizing the benefits of the lunar environment and mitigating the risks associated with material cohesion.

5.3. Limitations

This research, while providing a valid numerical framework for predicting material behavior in reduced gravity environments, has some intrinsic limitations arising from the simplifications adopted in the computational model. First, the numerical approach based on the PFEM treats fresh concrete as a homogeneous and continuous single-phase fluid. This assumption, although necessary to handle the large deformations typical of the extrusion process, neglects the two-phase physical nature of the material, consisting of a fluid matrix and discrete granular aggregates, which in reality could locally influence the flow and interaction between the layers. Furthermore, the governing equations of the model assume that the fluid is isothermal and incompressible, thus not taking into account density variations or alterations in rheological properties due to heat exchange during the deposition process.

A second substantial limitation concerns the partial reproduction of lunar environmental conditions. Although the study successfully isolated the effect of reduced gravitational acceleration ($1.62 m/s^2$), the simulations assume a stable environment and do not integrate other critical factors described in the preliminary analysis, such as the absence of atmosphere and the extreme thermal cycles. While the current model focuses on the mechanical stability of the flow, it does not simulate the thermodynamic changes that, in a real scenario, would induce rapid variations in viscosity and curing times due to vacuum exposure and radiation.

Finally, analyses were conducted on elementary test geometries, such as the superposition

of straight filaments and the construction of simple inclined walls, in order to validate the process parameters. The study did not extend to the simulation of complex architectural forms or the interaction with automated structural reinforcements, limiting the results to the validation of the deposition process rather than the structural performance of a complete habitat. It is also important to note that, given the current impossibility of conducting in situ experiments, the results are based exclusively on numerical validations and literature data relating to terrestrial regolith simulants, thus lacking direct experimental confirmation in the real lunar operating environment.

5.4. Future developments

Although numerical simulations conducted using the PFEM have provided promising results regarding the influence of lunar gravity and layer pressing, the present work relied on simplified environmental conditions to isolate mechanical variables. Consequently, the natural lines of research for the future development of this thesis are oriented towards greater simulation fidelity with respect to the extraterrestrial environment and towards increasing geometric complexity.

First, the integration of multiphysics models coupling fluid dynamics with thermodynamics is essential. Current simulations have considered the rheology of the material (via the Bingham and Saramito models) to be mainly stress- and time-dependent, but in a real lunar scenario, the absence of atmosphere and extreme temperature variations (with day-night cycles) play a crucial role. Future developments should therefore aim to couple PFEM with heat transfer and evaporation equations to explicitly model the "flash setting" phenomenon caused by vacuum-induced sublimation. This would allow for the prediction of how the rapid evolution of material stiffness influences interlayer adhesion and delamination risk under realistic thermal conditions.

Second, advanced optimization of process parameters is recommended. While this study identified layer pressing as the most effective strategy, further analysis is needed to quantitatively define the ideal operating windows. The use of optimization algorithms could allow the extrusion speed and nozzle height to be dynamically calibrated as a function of

rheological variations in real time, maximizing construction speed without compromising structural stability.

Finally, research will need to evolve from current simple wall geometries towards habitable structural typologies. Future simulations will need to test the printability of pressurized shell structures, domes, or cantilevered elements (overhangs), typical of lunar habitats designed to provide effective radiation protection. In parallel, it will be necessary to numerically investigate the fluid-structure interaction regarding the insertion of reinforcements during the printing process. Simulating the integration of fibers or bars into the fluid matrix would represent a decisive step in validating the engineering feasibility of habitable and resilient lunar infrastructures.

Bibliography

[1] Suvash Chandra Paul, Gideon P.A.G. van Zijl, Ming Jen Tan, and Ian Gibson. A review of 3d concrete printing systems and materials properties: current status and future research prospects. *Rapid Prototyping Journal*, 24(4):784–798, 2018. ISSN 1355-2546. doi: https://doi.org/10.1108/RPJ-09-2016-0154. URL `https://www.sciencedirect.com/science/article/pii/S135525461800188X`.

[2] Marjolein P.A.M. Marijnissen and Aant van der Zee. 3d concrete printing in architecture: A research on the potential benefits of 3d concrete printing in architecture. 2:299–308, 2017.

[3] Giedrius Girskas and Modestas Kligys. 3d concrete printing review: Equipment, materials, mix design, and properties. *Buildings*, 2025. URL `https://api.semanticscholar.org/CorpusID:279552714`.

[4] A. R. Krishnaraja and K. V. Guru. 3d printing concrete: A review. *IOP Conference Series: Materials Science and Engineering*, 1055(1):012033, 2021. doi: 10.1088/1757-899X/1055/1/012033.

[5] Bharat Bhushan Jindal and Parveen Jangra. 3d printed concrete: Acomprehensive review ofraw material's properties, synthesis, performance, andpotential field applications. *Construction and Building Materials*, 387:131614, 2023. ISSN 0950-0618. doi: https://doi.org/10.1016/j.conbuildmat.2023.131614. URL `https://www.sciencedirect.com/science/article/pii/S0950061823013272`.

[6] Narinder Singh, Francesco Colangelo, and Ilenia Farina. Sustainable non-conventional concrete 3d printing—a review. *Sustainability*, 15:10121, 06 2023. doi: 10.3390/su151310121.

[7] R. J. M. Wolfs and A. S. J. Suiker. Structural failure during extrusion-based 3d printing processes. *The International Journal of Advanced Manufacturing Technology*, 104(1-4):565–584, 2019. doi: 10.1007/s00170-019-03844-6.

[8] Wes McGee, Tsz Yan Ng, Kequan Yu, and Victor C. Li. Extrusion nozzle shaping for improved 3DP of engineered cementitious composites (ECC/SHCC). In F. P. Bos et al., editors, *DC 2020*, volume 28 of *RILEM Bookseries*, pages 916–925. Springer, 2020. doi: 10.1007/978-3-030-49916-7_89.

[9] Ghafur H. Ahmed, Nasih H. Askandar, and Ghazi B. Jumaa. A review of largescale 3dcp: Material characteristics, mix design, printing process, and reinforcement strategies. *Structures*, 43:508–532, 2022. ISSN 2352-0124. doi: https://doi.org/10.1016/j.istruc.2022.06.068. URL `https://www.sciencedirect.com/science/article/pii/S2352012422005483`.

[10] Liming Yang, Samad M.E. Sepasgozar, Sara Shirowzhan, Alireza Kashani, and David Edwards. Nozzle criteria for enhancing extrudability, buildability and interlayer bonding in 3d printing concrete. *Automation in Construction*, 146:104671, 2023. ISSN 0926-5805. doi: https://doi.org/10.1016/j.autcon.2022.104671. URL `https://www.sciencedirect.com/science/article/pii/S0926580522005416`.

[11] Atta Ur Rehman and Jung-Hoon Kim. 3d concrete printing: A systematic review of rheology, mix designs, mechanical, microstructural, and durability characteristics. *Materials*, 14(14):3800, 2021. doi: 10.3390/ma14143800.

[12] Norhafizah Salleh, Nur Syahera Jamalulail, Noor Azlina Abdul Hamid, Zalipah Jamellodin, Masni A. Majid, and Nurul Huda Suliman. New technology in 3D concrete printing by using ground granulated blast-furnace slag: A review. *IOP Conference Series: Materials Science and Engineering*, 1200(1):012007, 2021. doi: 10.1088/1757-899X/1200/1/012007.

[13] Domenico Asprone, Ferdinando Auricchio, Costantino Menna, and Valentino Mercuri. 3d printing of reinforced concrete elements: Technology and design approach. *Construction and Building Materials*, 165:218–231, 2018. doi: 10.1016/j.conbuildmat.2018.01.018.

[14] Xiaonan Wang, Wengui Li, Yipu Guo, Alireza Kashani, Kejin Wang, Liberato Ferrara, and Isabel Agudelo. Concrete 3d printing technology for sustainable construction: A review on raw material, concrete type and performance. *Developments in the Built Environment*, 17:100378, 2024. ISSN 2666-1659. doi: https://doi.org/10.1016/j.dibe.2024.100378. URL `https://www.sciencedirect.com/science/article/pii/S2666165924000590`.

[15] Zibo Zuo, Yamei Zhang, Jin Li, Yulin Huang, Longlong Zhang, Xianggang Wang, Yaxin Tao, and Wouter De Corte. Systematic workflow for digital design and on-site 3d printing of large concrete structures: A case study of a full-size two-story building. *Journal of Building Engineering*, 104:112370, 2025. ISSN 2352-7102. doi: https://doi.org/10.1016/j.jobe.2025.112370. URL `https://www.sciencedirect.com/science/article/pii/S2352710225006072`.

[16] Musa Alawneh, Motasem Matarneh, and Sameh El-Ashri. The world's first 3d-printed office building in dubai. 2018.

[17] Zeeshan Y. Ahmed, Rob J.M. Wolfs, Freek P. Bos, and Theo A.M. Salet. A framework for large-scale structural applications of 3d printed concrete: the case of a 29 m bridge in the netherlands. *Open Conference Proceedings*, 1:5–19, 2022. doi: 10.52825/ocp.v1i.74.

[18] A. Sgambati, M. Berg, F. Rossi, A. Daurskikh, B. Imhof, R. Davenport, P. Weiss, M. Peer, T. Gobert, and A. Makaya. URBAN: conceiving a lunar base using 3D printing technologies. (IAC-18-D3.3.7), 2018.

[19] Neil Leach. 3d printing in space. *Architectural Design*, 84(6):108–113, 2014. doi: 10.1002/ad.1840.

[20] Serdar Ulubeyli. Lunar shelter construction issues: The state-of-the-art towards 3d printing technologies. *Acta Astronautica*, 195:318–343, 2022. doi: 10.1016/j.actaastro.2022.03.033.

[21] Silvia Benvenuti, Fabio Ceccanti, and Xavier De Kestelier. Living on the moon: Topological optimization of a 3d-printed lunar shelter. *Nexus Network Journal*, 15 (2):285–302, 2013. doi: 10.1007/s00004-013-0155-7.

[22] F. Ceccanti, E. Dini, X. De Kestelier, V. Colla, and L. Pambaguian. 3D Printing Technology for a Moon Outpost Exploiting Lunar Soil. (IAC-10-D3.3.5), 2010.

[23] Adam E. Jakus, Katie D. Koube, Nicholas R. Geisendorfer, and Ramille N. Shah. Robust and elastic lunar and martian structures from 3d-printed regolith inks. *Scientific Reports*, 7(1):44931, 2017. doi: 10.1038/srep44931.

[24] Valentina Colla, Giovanni Cesaretti, Enrico Dini, Xavier De Kestelier, and Laurent Pambaguian. Monitoring concepts for a 3d printer applied to build a human outpost on the moon. pages 205–210, 2014. doi: 10.1109/UKSim.2014.50.

[25] Sebastian Wilhelm and Manfred Curbach. Review of possible mineral materials and production techniques for a building material on the moon. *Structural Concrete*, 15 (3):419–428, 2014. doi: 10.1002/suco.201300088.

[26] Sung Won Koh, Jaemin Yoo, Leonhard E. Bernold, and Tai Sik Lee. Experimental study of waterless concrete for lunar construction. pages 1098–1102, 2010. doi: 10.1061/41096(366)102.

[27] Ian P. Madden, Sathyashri Muruganandam, Amine Missaoui, Oliver Gries, Jonathan Kollmer, Olfa D'Angelo, and Suman Sinha-Ray. Rheology of lunar regolith simulant under varying gravitational conditions. *npj Microgravity*, 2025. doi: 10.1038/s41526-025-00501-z.

[28] Xiaowei Zheng, Cong Zhao, Xiaoyan Sun, and Weiwei Dong. Lunar regolith geopolymer concrete for in-situ construction of lunar bases: A review. *Polymers*, 16(11), 2024. doi: 10.3390/polym16111582.

[29] Khalid A. Alshibli and Alsidqi Hasan. Strength properties of jsc-1a lunar regolith simulant. *Journal of Geotechnical and Geoenvironmental Engineering*, 135(5):673–679, 2009. doi: 10.1061/(ASCE)GT.1943-5606.0000068.

[30] James Bowen, Vibha Levin Prabhu, Sungwoo Lim, and Mahesh Anand. The viscosity and processing of molten lunar regolith. *Scientific Reports*, 15(1):3938, 2025. doi: 10.1038/s41598-025-87761-7.

[31] Athanasios Goulas, Jon G. P. Binner, Daniel S. Engstrom, Russell A. Harris,

and Ross J. Friel. Mechanical behaviour of additively manufactured lunar regolith simulant components. *Proceedings of the Institution of Mechanical Engineers, Part L: Journal of Materials: Design and Applications*, 233(1):16–29, 2019. doi: 10.1177/1464420718755216.

[32] B. Reitz, C. Lotz, N. Gerdes, S. Linke, E. Olsen, K. Pflieger, S. Sohrt, M. Ernst, P. Taschner, J. Neumann, E. Stoll, and L. Overmeyer. Additive manufacturing under lunar gravity and microgravity. *Microgravity Science and Technology*, 33(2), 2021. doi: 10.1007/s12217-021-09878-4.

[33] Yifan Sun, Siqi Ma, Qingze Chen, Guoliang Chen, Yaming Wang, Jun Qiu, Dechang Jia, and Peigang He. Lunar regolith simulant-derived 3d-printed geopolymers with optimized mechanical and thermal management properties. *Composites Part A: Applied Science and Manufacturing*, 196:108989, 2025.

[34] Christopher Duffey, M. Lea, and J. Brisset. Measuring regolith strength in reduced gravity environments in the laboratory. *arXiv preprint arXiv:2411.11571*, 2024. URL `https://arxiv.org/abs/2411.11571`.

[35] Wucheng Sun, Fen Dang, Yan Zhou, Shifeng Wen, Cheng Zhou, Yusheng Shi, and Lieyun Ding. Additive manufacturing of lunar regolith: A review. *Additive Manufacturing Frontiers*, 4:200225, 2025. doi: 10.1016/j.amf.2025.200225.

[36] Laura Ricciotti, Antonio Apicella, Valeria Perrotta, and Raffaella Aversa. Geopolymer materials for extrusion-based 3d-printing: A review. *Polymers*, 15(24), 2023. doi: 10.3390/polym15244688.

[37] Feng Li, Rongrong Zhang, Siqi Zhou, and Xingyi Zhu. Printability and hardening performance of three-dimensionally-printed geopolymer based on lunar regolith simulant for automated construction of lunar infrastructure. *Frontiers of Structural and Civil Engineering*, 17(10):1535–1553, 2023. doi: 10.1007/s11709-023-0003-0.

[38] Giacomo Rizzieri, Liberato Ferrara, and Massimiliano Cremonesi. Numerical simulation of the extrusion and layer deposition processes in 3d concrete printing with the particle finite element method. *Computational Mechanics*, 73:277–295, 2024. doi: 10.1007/s00466-023-02367-y.

[39] Nicolas Roussel, Annika Gram, Massimiliano Cremonesi, Liberato Ferrara, Knut Krenzer, Viktor Mechtcherine, Sergiy Shyshko, Jan Skocec, Jon Spangenberg, Oldrich Svec, Lars Nyholm Thrane, and Ksenija Vasilic. Numerical simulations of concrete flow: A benchmark comparison. *Cement and Concrete Research*, 79:265–271, 2016. ISSN 0008-8846. doi: https://doi.org/10.1016/j.cemconres.2015.09.022. URL https://www.sciencedirect.com/science/article/pii/S0008884615002604.

[40] Nicolas Roussel, Mette R. Geiker, Frédéric Dufour, Lars N. Thrane, and Peter Szabo. Computational modeling of concrete flow: General overview. *Cement and Concrete Research*, 37(9):1298–1307, 2007. ISSN 0008-8846. doi: https://doi.org/10.1016/j.cemconres.2007.06.007. URL https://www.sciencedirect.com/science/article/pii/S0008884607001366.

[41] Phillip Banfill. Rheology of fresh cement and concrete. *Rheol Rev*, 01 1991. doi: 10.4324/9780203473290.

[42] Pierre Saramito. A new constitutive equation for elastoviscoplastic fluid flows. *Journal of Non-Newtonian Fluid Mechanics*, 145(1):1–14, 2007. ISSN 0377-0257. doi: https://doi.org/10.1016/j.jnnfm.2007.04.004. URL https://www.sciencedirect.com/science/article/pii/S0377025707000869.

[43] Pierre Saramito. A new elastoviscoplastic model based on the herschel–bulkley viscoplastic model. *Journal of Non-Newtonian Fluid Mechanics*, 158(1):154–161, 2009. ISSN 0377-0257. doi: https://doi.org/10.1016/j.jnnfm.2008.12.001. URL https://www.sciencedirect.com/science/article/pii/S0377025708002267. Viscoplastic fluids: From theory to application.

[44] Giacomo Rizzieri, Liberato Ferrara, and Massimiliano Cremonesi. A partitioned lagrangian finite element approach for the simulation of viscoelastic and elastoviscoplastic free-surface flows. *Computer Methods in Applied Mechanics and Engineering*, 443:118071, 2025. ISSN 0045-7825. doi: https://doi.org/10.1016/j.cma.2025.118071. URL https://www.sciencedirect.com/science/article/pii/S0045782525003433.

[45] Massimiliano Cremonesi, Alessandro Franci, Sergio Idelsohn, and Eugenio Oñate.

A state of the art review of the particle finite element method (pfem). *Archives of Computational Methods in Engineering*, 27:1709–1735, 2020. doi: 10.1007/s11831-020-09468-4.

[46] Giacomo Rizzieri, Massimiliano Cremonesi, and Liberato Ferrara. A 2d numerical model of 3d concrete printing including thixotropy. *Materials Today: Proceedings*, 2023. ISSN 2214-7853. doi: https://doi.org/10.1016/j.matpr.2023.08.082. URL https://www.sciencedirect.com/science/article/pii/S2214785323043353.

[47] Georgia Kimbell and Mohammad A. Azad. Chapter fifteen - 3d printing: Bioinspired materials for drug delivery. In Md Nurunnabi, editor, *Bioinspired and Biomimetic Materials for Drug Delivery*, Woodhead Publishing Series in Biomaterials, pages 295–318. Woodhead Publishing, 2021. ISBN 978-0-12-821352-0. doi: https://doi.org/10.1016/B978-0-12-821352-0.00011-3. URL https://www.sciencedirect.com/science/article/pii/B9780128213520000113.

[48] V. Mechtcherine, F.P. Bos, A. Perrot, W.R. Leal da Silva, V.N. Nerella, S. Fataei, R.J.M. Wolfs, M. Sonebi, and N. Roussel. Extrusion-based additive manufacturing with cement-based materials – production steps, processes, and their underlying physics: A review. *Cement and Concrete Research*, 132:106037, 2020. ISSN 0008-8846. doi: https://doi.org/10.1016/j.cemconres.2020.106037. URL https://www.sciencedirect.com/science/article/pii/S0008884619317132.

[49] Britannica Editors. Shear modulus. https://www.britannica.com/science/shear-modulus, December 2025. Last updated Dec. 22, 2025; accessed Feb. 2, 2026.

[50] Giacomo Rizzieri, Simone Meni, Massimiliano Cremonesi, and Liberato Ferrara. A particle finite element method for investigating the influence of material and process parameters in 3d concrete printing. *Computers Structures*, 316:107883, 2025. ISSN 0045-7949. doi: https://doi.org/10.1016/j.compstruc.2025.107883. URL https://www.sciencedirect.com/science/article/pii/S004579492500241X.

[51] Alexandra Marnot, Katie Koube, Sungwoo Jang, Naresh Thadhani, Josh Kacher, and Blair Brettmann. Material extrusion additive manufacturing of high particle loaded

suspensions: a review of materials, processes and challenges. *Virtual and Physical Prototyping*, 18(1):e2279149, 2023. doi: 10.1080/17452759.2023.2279149.

[52] Nicolas Roussel. Rheological requirements for printable concretes. *Cement and Concrete Research*, 112:76–85, 2018. ISSN 0008-8846. doi: https://doi.org/10.1016/j.cemconres.2018.04.005. URL https://www.sciencedirect.com/science/article/pii/S000888461830070X. SI : Digital concrete 2018.

[53] Rob J. M. Wolfs, Freek P. Bos, and Theo A. M. Salet. Structural built-up of cement-based materials used for 3d printing. *Cement and Concrete Research*, 100:475–484, 2017. doi: 10.1016/j.cemconres.2017.05.011.

[54] Timothy Wangler, Nicolas Roussel, Freek P. Bos, Theo A. M. Salet, and Robert J. Flatt. Digital concrete: A review. *RILEM Technical Letters*, 1:67–75, 2016. doi: 10.21809/rilemtechlett.2016.16.

[55] Jacques Kruger, Stephan Zeranka, and Gideon van Zijl. 3d concrete printing: A lower bound analytical model for buildability performance quantification. *Automation in Construction*, 106:102904, 2019. ISSN 0926-5805. doi: https://doi.org/10.1016/j.autcon.2019.102904. URL https://www.sciencedirect.com/science/article/pii/S0926580519301852.

[56] R.J.M. Wolfs, F.P. Bos, and T.A.M. Salet. Early age mechanical behaviour of 3d printed concrete: Numerical modelling and experimental testing. *Cement and Concrete Research*, 106:103–116, 2018. ISSN 0008-8846. doi: https://doi.org/10.1016/j.cemconres.2018.02.001. URL https://www.sciencedirect.com/science/article/pii/S000888461730532X.

[57] Yu Zhang, Yunsheng Zhang, Wei She, Lin Yang, Guojian Liu, and Yonggan Yang. Rheological and harden properties of the high-thixotropy 3d printing concrete. *Construction and Building Materials*, 201:278–285, 2019. ISSN 0950-0618. doi: https://doi.org/10.1016/j.conbuildmat.2018.12.061. URL https://www.sciencedirect.com/science/article/pii/S0950061818330356.

List of Figures

List of Tables